

# Self-consistent description of multipole strength: systematic calculations

J. Terasaki

*School of Physics, Peking University, Beijing 100871, P. R. China*

J. Engel

*Department of Physics and Astronomy,  
University of North Carolina, Chapel Hill, NC 27599-3255*

(Dated: July 4, 2018)

## Abstract

We use the quasiparticle random phase approximation with a few Skyrme density functionals to calculate strength functions in the  $J^\pi = 0^+, 1^-$ , and  $2^+$  channels for even Ca, Ni, and Sn isotopes, from the proton drip line to the neutron drip line. We show where and how low-lying strength begins to appear as  $N$  increases. We also exhibit partial energy-weighted sums of the transition strength as functions of  $N$  for all nuclei calculated, and transition densities for many of the interesting peaks.

We find that low-energy strength increases with  $N$  in all multipoles, but with distinctive features in each. The low-lying  $0^+$  strength near the neutron at large  $N$  barely involves protons at all, with the strength coming primarily from a single two-quasineutron configuration with very large spatial extent. The low-lying  $1^-$  strength is different, with protons contributing to the transition density in the nuclear interior together with neutrons at large radii. The low-lying  $2^+$  transition strength goes largely to more localized states. The three Skyrme interactions we test produce similar results, differing most significantly in their predictions for the location of the neutron drip line, the boundaries of deformed regions, energies of and transition strengths to the lowest  $2^+$  states between closed shells, and isovector energy-weighted sum rules.

PACS numbers: 21.10.Pc, 21.60.Jz

## I. INTRODUCTION

Very unstable nuclei with unusual ratios of neutron number ( $N$ ) to proton number ( $Z$ ) are currently the subject of intense theoretical and experimental work. A particularly important issue is the effect on nuclear properties of a large neutron excess and the accompanying low-lying continuum of excited states. In ground states these conditions sometimes lead to halos, thick skins, and changes in magic numbers. Less is known about excited states, which we study here by calculating transition strengths and densities.

Most of the work on excited states is in light neutron-rich nuclei; a low-energy strength-function peak has been studied for years. Recent work [1–3] has focused on enhanced  $1^-$  strength in nuclei like  $^{11}\text{Li}$  or in neutron-rich oxygen isotopes [4–12]. But in heavier nuclei, calculations are more spotty. Several groups have calculated the isovector (IV)  $1^-$  strength functions, or photoabsorption cross sections, in the Ca isotopes [6, 11, 13–15]. References [6, 15] predict a small peak at around  $E = 9$  MeV in  $^{60}\text{Ca}$ . The first paper also calculates the strength function in  $^{48}\text{Ca}$ , finding no low-energy peak, but Ref. [14], a calculation based on density-functional theory, finds a very broad bump at  $E = 6$ –10 MeV. It is not clear, therefore, at what value of  $N$  the low-energy strength is first discernible.

The method we use here, the quasiparticle random phase approximation (QRPA), has been applied mainly to selected  $1^-$  excitations in particular isotopes of O, Ca, and Ni; one example is Ref. [11], which asserts that the low-energy excitations reflect strong particle-particle (“dineutron”) correlations. References [16, 17] show extensive and systematic QRPA calculations of photoabsorption cross sections, but focus primarily on radiative neutron-capture cross sections. The relativistic QRPA [9, 18–20] has been applied more with an eye to nuclear structure issues (for a recent review, see Ref. [21]), asserting, for example, that low-lying isoscalar (IS)  $1^-$  states exhibit toroidal flow. References [22, 23] go beyond RPA, altering details of predicted low-lying strength.

Other channels have been discussed less than the IV  $1^-$ . The authors of Ref. [24] calculate  $0^+$  strength functions in Ca isotopes up to the neutron drip line, finding an enhancement at low energy in  $^{60}\text{Ca}$ . Reference [25] examines transition strengths in the  $0^+$ ,  $1^-$ , and  $2^+$  channels near the neutron drip line, finding, for example, a sharp  $2^+$  peak near  $E = 0$  in  $^{110}\text{Ni}$ .

The above represents a considerable amount of work on excitations in exotic nuclei. Its range and results can be summarized, roughly, as follows: 1) Most of the calculations are for spherical nuclei, and the IV  $1^-$  channel has been studied the most. 2) A low-energy peak grows as  $N$  increases. 3) The low-energy excitations do not seem collective in the  $1^-$  channel (e.g. Ref. [26]), i.e. they do not contain more than a few particle-hole or two-quasiparticle configurations. 4) The corresponding transition densities have long neutron tails extending beyond the bulk nuclear radius. 5) The neutron skin thickness is correlated with the amount of low-energy strength [27]. 6) Calculations reproduce measurements of the amount of low-energy strength fairly well if they include many-particle many-hole correlations [22, 23].

Most of this work has focused on nuclei right at the drip line and, as already noted, has emphasized the IV  $1^-$  channel. It is still not known whether theory makes similar predictions for other neutron-rich nuclei, or to what extent the properties of the low-energy peaks vary from one multipole to another. The purpose of this paper, therefore, is to calculate strength functions in as many nuclei as possible, in all multipoles up to  $2^+$ , and investigate how the properties of the strength functions vary as  $N$  and the multipolarity change. We use the QRPA with Skyrme density functionals (which we refer to as interactions from here on) and

volume-type delta pairing interactions.

Currently, the QRPA is the most sophisticated method that can be used systematically for resonances of all energies in heavy nuclei without assuming that part of the nucleus forms an inert core. Here we will display results of QRPA calculations for Ca, Ni, and Sn isotopes from the proton drip line to the neutron drip line, describing the corresponding strength functions and transition densities in detail. We will also examine whether results depend on which Skyrme interaction we use, so that we can identify important measurements/nuclei that will help distinguish among them.

Section II below describes our method. Section III shows strength functions in the three isotopic chains and looks for  $(N, Z)$ -dependent trends in their behavior. Section IV discusses transition densities to states in low-lying peaks. Section V is a conclusion.

## II. CALCULATION

Our approach to the QRPA is described in detail in Ref. [28], and we discuss it here only briefly. The starting point is a coordinate-space Hartree-Fock-Bogoliubov (HFB) calculation, carried out with the code used in Refs. [29, 30]. The code outputs quasiparticle wave functions, with spherical symmetry assumed. It takes the continuum into account by placing the nucleus in a 20-fm box. We use as large a single-particle space as possible and solve the HFB equations accurately, so as to ease the removal of spurious states from the QRPA and satisfy sum rules.

We diagonalize the HFB density matrix to obtain a set of canonical states — as many as there are quasiparticle states — that make up our QRPA basis. The QRPA-Hamiltonian matrix then contains off-diagonal elements from the quasiparticle one-body Hamiltonian as well as the matrix elements of the residual two-body interaction. The two-body matrix elements are functional derivatives of the energy with respect to the density and pairing tensor. After diagonalizing the QRPA Hamiltonian, we use the eigenvectors to obtain strength functions [31] and transition densities (see Appendix).

We cannot handle an infinite number of canonical quasiparticle states, and so truncate our basis in the following way: For  $N < 82$  the maximum single-particle angular momentum  $j_{\max}$  is  $15/2$ , and for  $N \geq 84$   $j_{\max}$  is  $21/2$ . If the ground state has a finite pairing gap in the HFB calculation we truncate the canonical quasiparticle basis in the QRPA by omitting states with very small occupation probability  $v_i^2$ . In the  $J^\pi = 0^+$  and  $1^-$  channel we keep states with  $v_i^2 \geq 10^{-12}$ , and in the  $J^\pi = 2^+$  channel we keep those with  $v_i^2 \geq 10^{-8}$ . If the mean field has no pairing we use the Hartree-Fock energy to truncate; in the  $J^\pi = 0^+$  and  $1^-$  channels we keep single-particle states with energy  $\varepsilon_i \leq 150$  MeV, and in the  $J^\pi = 2^+$  channel we keep those with  $\varepsilon_i \leq 100$  MeV. In the HFB calculations we always cut off the quasiparticle spectrum at 200 MeV.

The largest QRPA-Hamiltonian matrix that we encounter here (in the  $1^-$  channel for Sn near the neutron drip line) is about 14,000, and the minimum is about 2,000 (in the  $0^+$  channel for Ca near the proton drip line).<sup>1</sup> The separation of spurious excitations from physical states is as complete as in Ref. [28] in most of cases.

We use 3 Skyrme interactions: SkM\*, SLy4, and SkP. Our pairing interaction has zero

---

<sup>1</sup> In Ref. [28], cut-offs of  $v_i^2 = 10^{-12}$  and  $\varepsilon_i = 150$  MeV were used for the  $2^+$  channel, and then the maximum dimension of the Hamiltonian matrix was about 20,000.

range with no density dependence (this is “volume pairing”). For reasons we do not understand, we cannot obtain solutions of the HFB equation with SkP for Ca and Ni isotopes. The other interactions give solutions that are unstable against QRPA quadrupole vibrations for isotopes with:  $N = 72$  in Ni (SkM\*);  $N = 104 - 112$  (SkM\*) and  $N = 60 - 64, 96 - 110$  (SLy4) in Sn, and so we do not discuss these nuclei.

### III. STRENGTH FUNCTIONS

Strength functions are important because they capture information about all excited states and can often be measured. We define the strength functions through the transition operators

$J^\pi = 0^+$ :

$$\begin{aligned}\hat{F}_{00}^{\text{IS}} &= \frac{eZ}{A} \sum_{i=1}^A r_i^2, \\ \hat{F}_{00}^{\text{IV}} &= \frac{eN}{A} \sum_{i=1}^Z r_i^2 - \frac{eZ}{A} \sum_{i=1}^N r_i^2,\end{aligned}\tag{1}$$

$J^\pi = 1^-$ :

$$\begin{aligned}\hat{F}_{1M}^{\text{IS}} &= \frac{eZ}{A} \sum_{i=1}^A r_i^3 Y_{1M}(\Omega_i), \\ \hat{F}_{1M}^{\text{IV}} &= \frac{eN}{A} \sum_{i=1}^Z r_i Y_{1M}(\Omega_i) - \frac{eZ}{A} \sum_{i=1}^N r_i Y_{1M}(\Omega_i),\end{aligned}\tag{2}$$

$J^\pi = 2^+$ :

$$\begin{aligned}\hat{F}_{2M}^{\text{IS}} &= \frac{eZ}{A} \sum_{i=1}^A r_i^2 Y_{2M}(\Omega_i), \\ \hat{F}_{2M}^{\text{IV}} &= \frac{eN}{A} \sum_{i=1}^Z r_i^2 Y_{2M}(\Omega_i) - \frac{eZ}{A} \sum_{i=1}^N r_i^2 Y_{2M}(\Omega_i),\end{aligned}\tag{3}$$

where  $A$  is total-nucleon number, and  $i$  is a single-particle index. The upper limit for  $Z$  ( $N$ ) on a summation sign means that the sum is over protons (neutrons).

In the next few sections we show the strength functions, with spurious states removed, produced by SkM\*, and discuss those produced by the other Skyrme interactions when appropriate. We then display energy-weighted sums (up to several different energies) produced by all our interactions, in all isotopes.

#### A. The $0^+$ channels

Figures 1–3 show the IS and IV strength functions in the  $J^\pi = 0^+$  channels. In Ca (Fig. 1), most of the functions are smooth except for small low-energy spikes in several

nuclei and the large low-energy peaks in  $^{74,76}\text{Ca}$ . The IS giant resonances peak at  $E = 20$  MeV for  $^{36-52}\text{Ca}$  and gradually move to 15 MeV by  $^{76}\text{Ca}$ . As  $N$  approaches the neutron drip line, a peak near  $E = 0$  grows, becoming quite large at the drip line. The IV giant resonance is broad in the light isotopes and develops a low-energy component as  $N$  increases, apparently increasing the summed strength. The larger peak varies only slightly in energy over the same range of  $N$ . Near the drip line the low-energy IV strength develops a peak that exactly mirrors the IS peak, indicating that the strength in both channels is produced solely by neutrons. This distinct low-energy bump seems to appear first at 10 MeV in  $^{50}\text{Ca}$ . This nucleus is not as short-lived as the isotopes near the drip line; perhaps the appearance of the low-energy mode is experimentally testable. The same nucleus marks the beginning of the low energy peak when we use SLy4.

The  $N$  dependence of the strength function of Ni (Fig. 2) is similar in many ways to that of Ca; the energy of the IS giant-resonance energy, for example, falls in a similar way past  $N = 40$ . A large low-energy peak again develops near the neutron-drip line, though not as dramatically as in Ca, and with the complication that the strength shrinks after  $^{90}\text{Ni}$ . This peak first is noticeable in both the IS and IV channel at 6 MeV in  $^{80}\text{Ni}$ , here and in calculations with SLy4. This example and that in Ca suggest more generally that the nucleus with 2 neutrons outside a closed shell will mark the appearance of the low-energy peak.

In Sn (Fig. 3), the peak near zero energy around the drip line is much smaller than in Ca and Ni. The bump first appears in  $^{136}\text{Sn}$  at  $E = 8$  MeV (violating by two nucleons the conjecture made a few lines up) in both the IS and IV channels. This threshold nucleus is the same with other Skyrme interactions.

Although we can make these kinds of comparisons in words, we would like to display the results of both (or all three where possible) Skyrme interactions in a more quantitative and graphic way. To limit the number of our figures, we do so by showing predictions for the sum of energy weighted strength up to 4 successively higher energies. We define the ‘‘partial’’ sum, up to an energy  $E$  as

$$W_E = \int_0^E dE' E' S(E'), \quad (4)$$

where  $S(E')$  is a strength function<sup>2</sup> (see Eq. (1) of Ref. [28]). Figure 4 shows  $W_E$  with  $E = 10, 20, 30,$  and  $100$  MeV for the IS  $0^+$  channel in Ca. All Skyrme interactions show similar  $N$ -dependence and  $E$ -dependence; the difference between the  $E = 30$  and  $100$  MeV curves is comparable with or smaller than the differences among the other curves (separated by 10 MeV), reflecting the eventual vanishing of the strength as  $E$  increases. The  $E = 20$  MeV curve increases more rapidly with  $N$  than the others in the region  $N > 30$ , indicating that the strength around  $E = 20$  MeV is shifted down at large  $N$ .

The differences among the interactions are most apparent in the location of the neutron drip line, a static property. The differences in strength functions, at least in this channel, are for the most part minor (though large enough to make significant differences in, e.g, the compression modulus).

---

<sup>2</sup> If the strength function has a large peak near  $E = 0$ , Eq. (4) overestimates the energy-weighted sum, because the tail in the negative energy region is not included. This problem occurs near the neutron drip line, and the energy-weighted sum is then overestimated by 10 % at most. We did not calculate  $W_E$  from negative  $E'$ , because then  $W_{10\text{MeV}}$  is sometimes negative.

Figure 5 shows the partial sums in the IV channel. Here the two interactions do yield somewhat different results. Though the  $N$ -dependence is similar, SkM\* produces more integrated strength than SLy4. To see how the total energy-weighted strength can differ from one interaction to another, we examine the IV energy-weighted sum rule (EWSR)

$$\sum_k \sum_M E_k |\langle k | \hat{F}_{JM}^{\text{IV}} | 0 \rangle|^2 = S_{\text{EW}}(J) + C_c I_c(J), \quad (5)$$

$$S_{\text{EW}}(0) = \frac{2e^2 \hbar^2}{m} \left\{ \frac{N^2 Z}{A^2} \langle r^2 \rangle_{\text{p}} + \frac{Z^2 N}{A^2} \langle r^2 \rangle_{\text{n}} \right\}, \quad (6)$$

$$S_{\text{EW}}(J \geq 1) = \frac{e^2 \hbar^2}{8\pi m} J(2J+1)^2 \left\{ \frac{N^2 Z}{A^2} \langle r^{2J-2} \rangle_{\text{p}} + \frac{Z^2 N}{A^2} \langle r^{2J-2} \rangle_{\text{n}} \right\}, \quad (7)$$

$$C_c = \frac{1}{4}(t_1 + t_2) + \frac{1}{8}(t_1 x_1 + t_2 x_2), \quad (8)$$

$$I_c(J) = e^2 \sum_M \int d^3 \mathbf{r} |\nabla f_{JM}(\mathbf{r})|^2 \rho_0^{\text{n}}(\mathbf{r}) \rho_0^{\text{p}}(\mathbf{r}), \quad (9)$$

$$f_{00}(\mathbf{r}) = r^2, \quad (10)$$

$$f_{JM}(\mathbf{r}) = r^J Y_{JM}(\Omega), \quad J \geq 1. \quad (11)$$

Here  $E_k$  is the energy of the excited state  $|k\rangle$ ,  $|0\rangle$  is the ground state,  $m$  is the nucleon mass, and  $\langle r^2 \rangle_{\text{p}}$  ( $\langle r^2 \rangle_{\text{n}}$ ) is the mean square proton (neutron) ground-state radius. The sum over states  $k$  does not include spurious states. The second term  $C_c I_c(J)$  in Eq. (5), with  $\rho_0^{\text{p}}(\mathbf{r})$  and  $\rho_0^{\text{n}}(\mathbf{r})$  of Eq. (9) the proton and neutron ground-state densities, is a correction arising from the momentum-dependent terms of the Skyrme interaction. The Skyrme parameters  $t_0, t_1, \dots$  are defined in Refs. [32] (SkM\*), [33] (SLy4), and [29] (SkP). Another term in the sum rule depending on the proton-neutron mixed density is always zero in our work.

In Tab. I we show  $S_{\text{EW}}(0)$ ,  $C_c$ ,  $I_c(0)$ , and EWSR (the full energy-weighted sum) for  $^{60}\text{Ca}$ . The interactions reproduce ground-state observables about equally well, so the difference in the EWSR, as the table shows, comes from the term involving  $C_c$ . The degree by which the EWSR exceeds  $S_{\text{EW}}(J)$  is in line with expectations (see, e.g., Chap. 10 of [34] and Refs. [33, 35]).

The properties of Ni are similar to those of Ca.  $W_{E=20\text{MeV}}$  in the IS channel of Ni increases more rapidly than the other curves (Fig. 6). SkM\* again has the larger IV sum-rule value. (Fig. 7).  $W_{E=20\text{MeV}}$  in the IS channel of Sn is much higher than  $W_{E=10\text{MeV}}$  (Fig. 8), reflecting the lower energy of the giant resonance. Figure 9 shows that the IV sum rules follow the same order as in the other isotopes, with SkP slightly larger than SLy4.

TABLE I: Components of the EWSR of IV  $0^+$  channel of  $^{60}\text{Ca}$ .

parameter set	$S_{\text{EW}}(0)$ ( $e^2\text{MeVfm}^4$ )	$C_c$ ( $\text{MeVfm}^5$ )	$I_c(0)$ ( $e^2/\text{fm}$ )	EWSR ( $e^2\text{MeVfm}^4$ )
SkM*	15587	68.74	58.01	19575
SLy4	15722	32.47	57.90	17602
SkP		44.64		

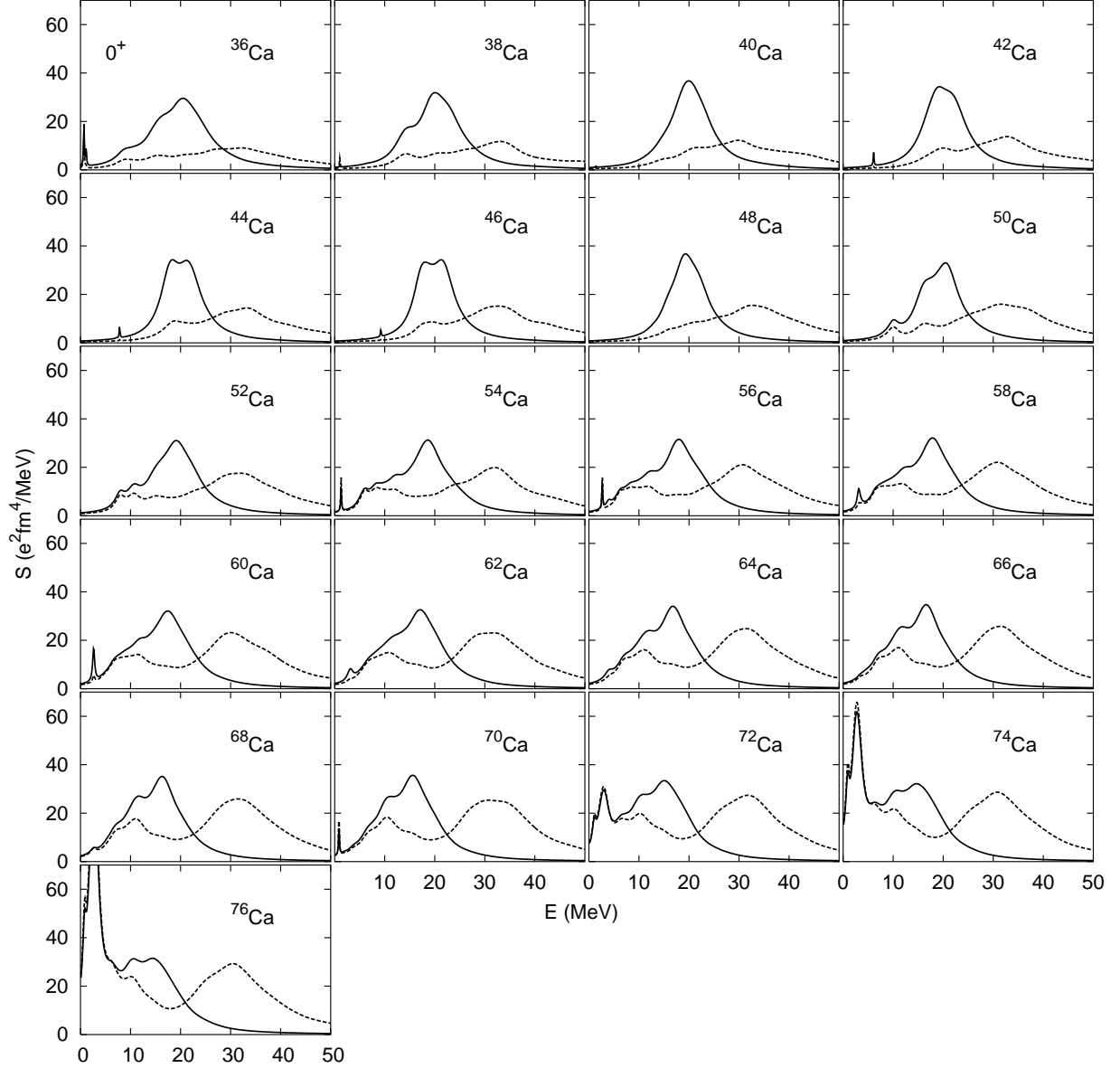


FIG. 1: IS (solid) and IV (dashed)  $0^+$  strength functions for even Ca isotopes (SkM\*).

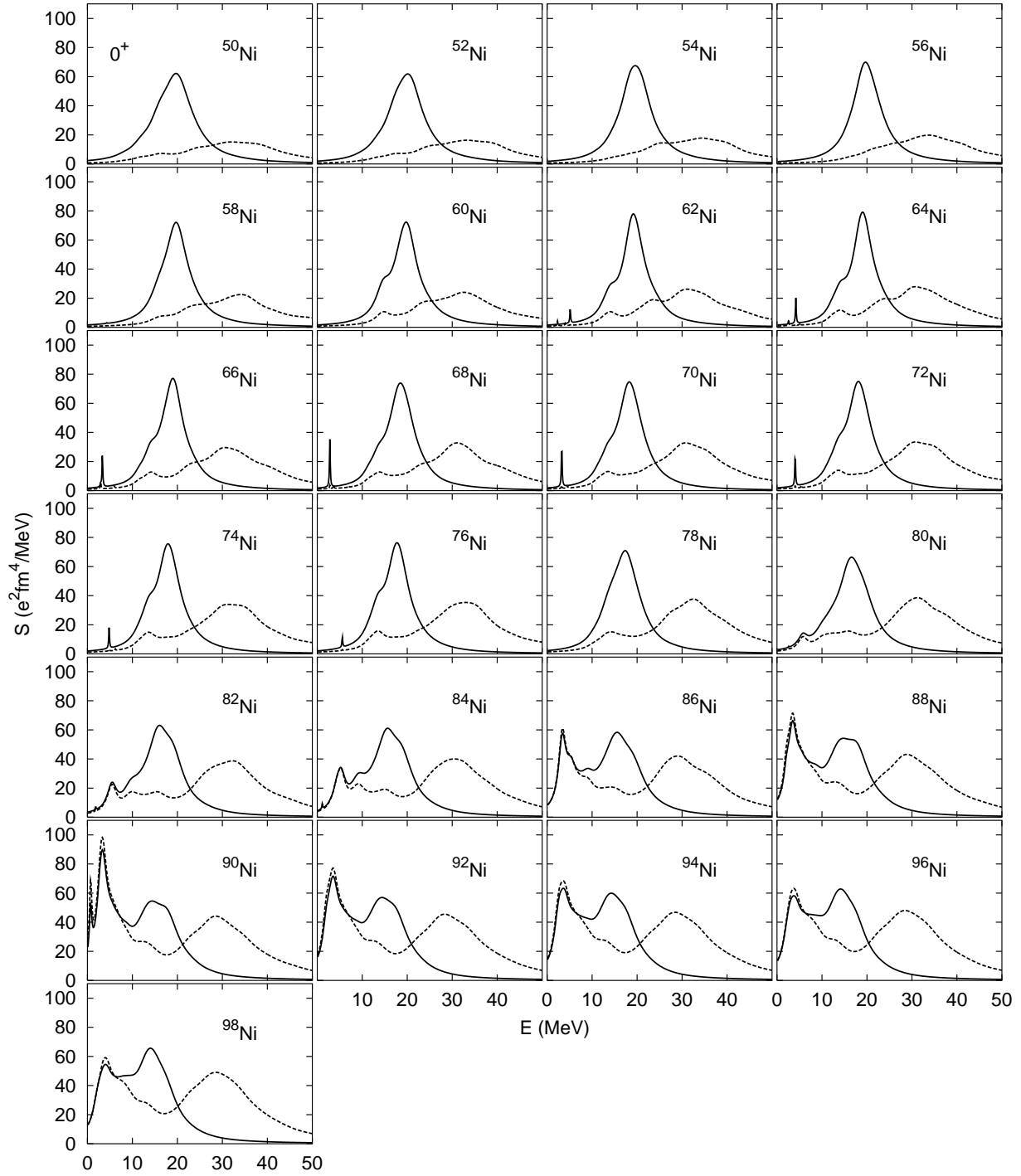


FIG. 2: The same as Fig. 1 but for Ni isotopes.



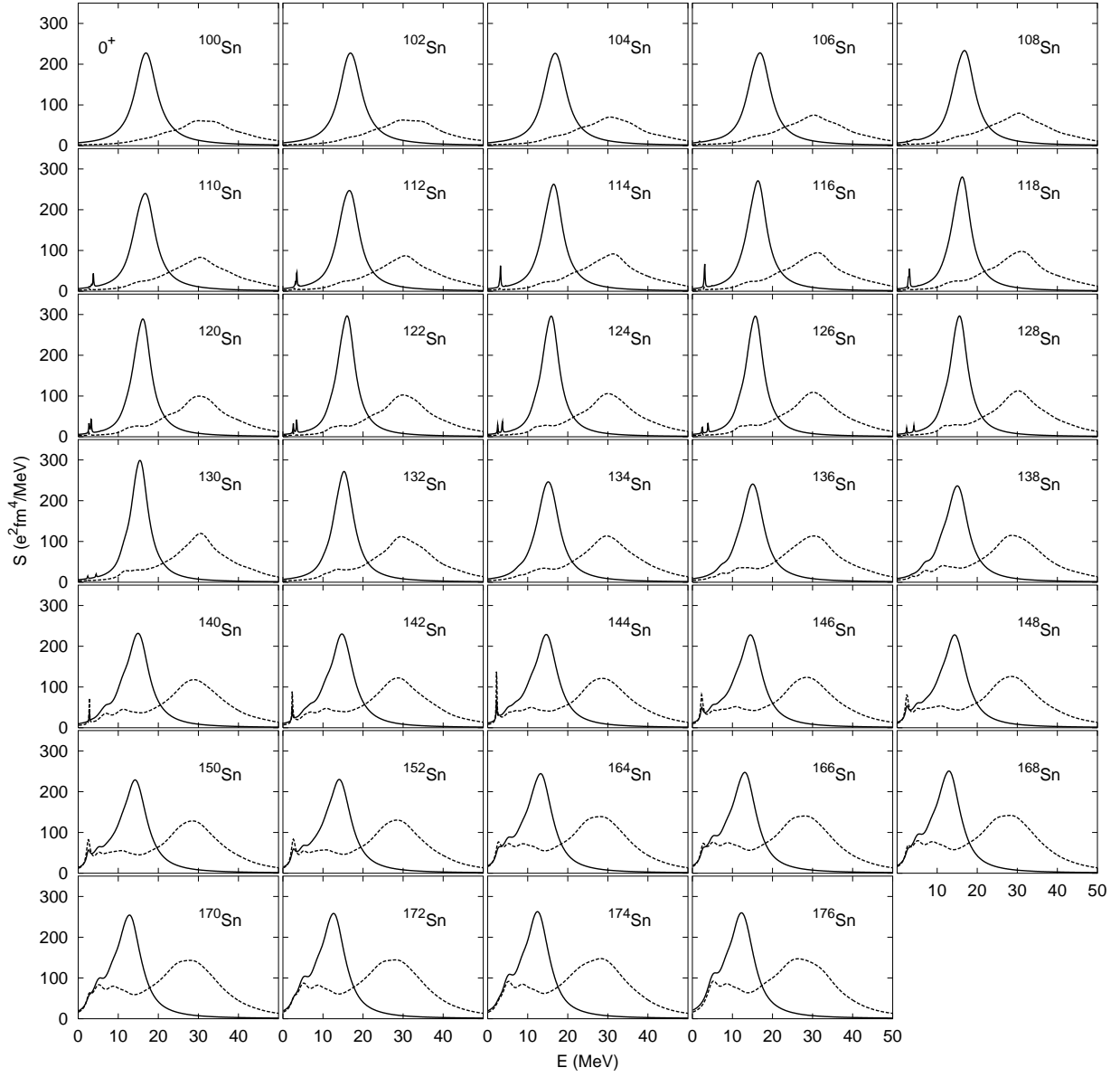


FIG. 3: The same as Fig. 1 but for Sn isotopes.

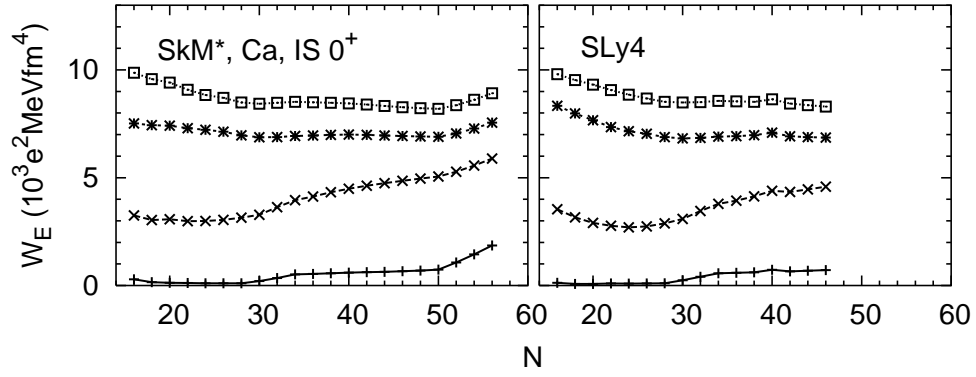


FIG. 4:  $N$ -dependence of the partial energy-weighted sums in the IS  $0^+$  channel of Ca. The upper limits of the sums are 10 MeV (plus symbol), 20 MeV (x), 30 MeV (asterisk), and 100 MeV (open square).

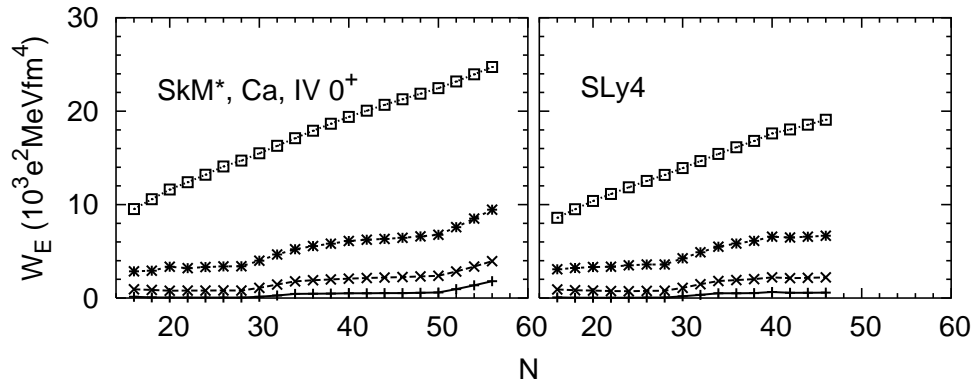


FIG. 5: The same as Fig. 4 but for the IV channel. The open squares now correspond to an upper limit of 150 MeV.

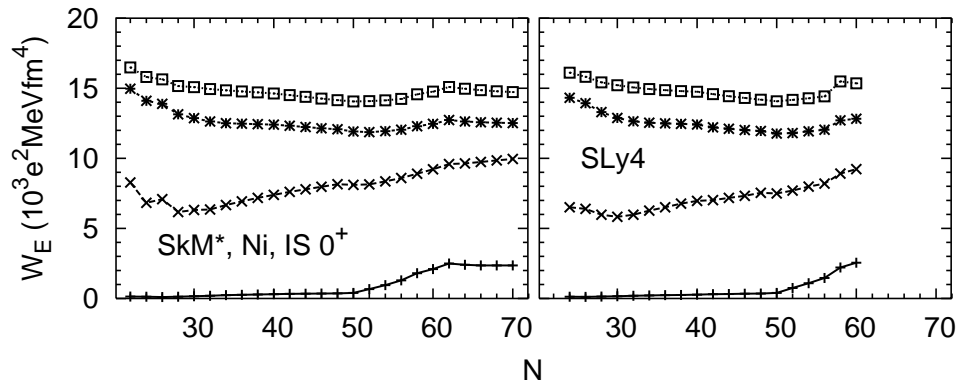


FIG. 6: The same as Fig. 4 but for Ni.

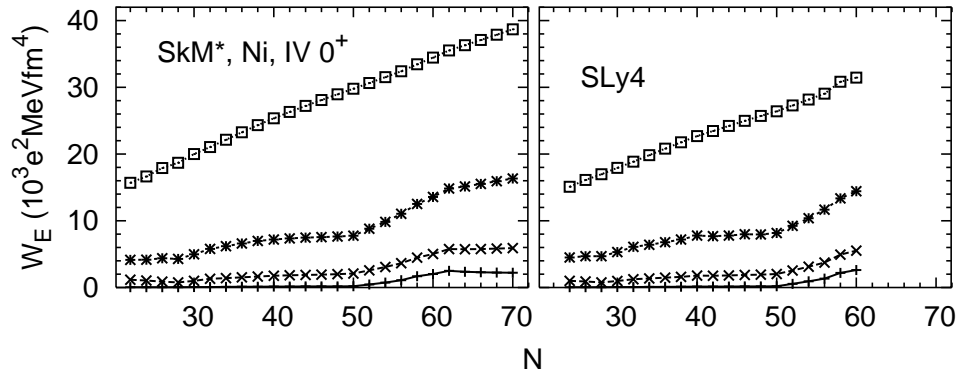


FIG. 7: The same as Fig. 5 but for Ni.

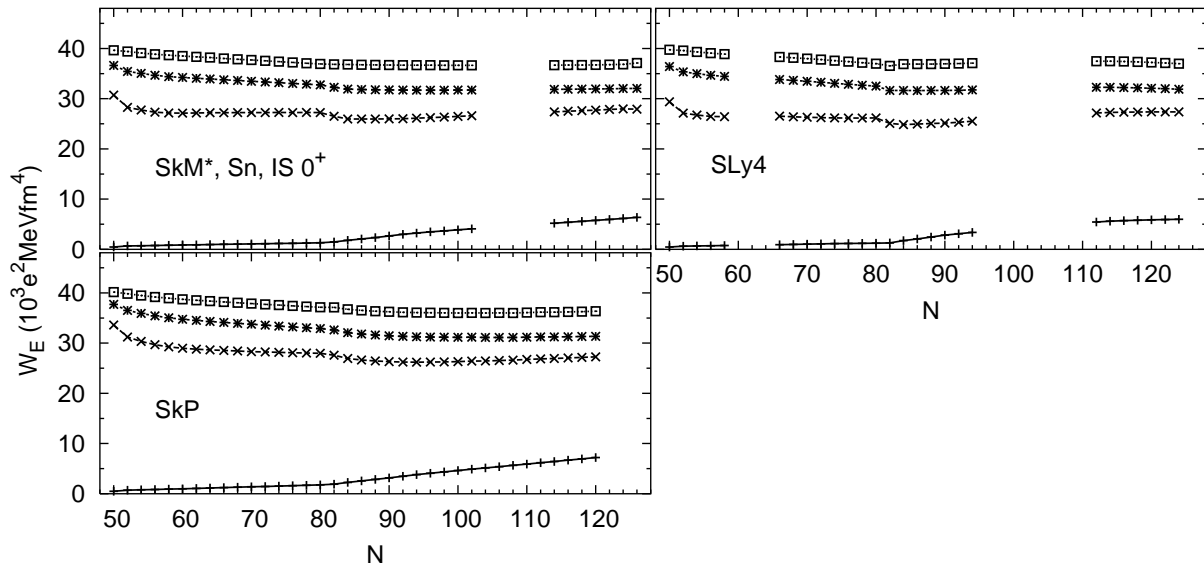


FIG. 8: The same as Fig. 4 but for Sn.

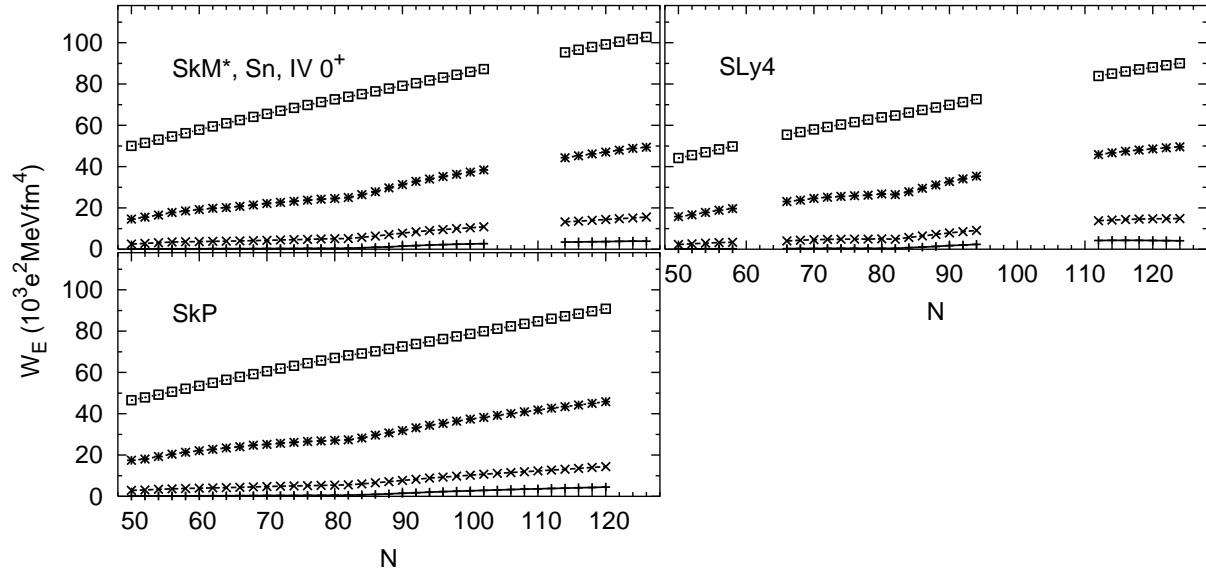


FIG. 9: The same as Fig. 5 but for Sn.

## B. The $1^-$ channels

Having analyzed the  $0^+$  strength functions in detail, we will, for the most part, let the higher-multipole figures speak for themselves. Just a few remarks about the  $1^-$  channel: The IS strength functions in Ca appear in Fig. 10. Here, unlike in the  $0^+$  channel, there is a clear low-energy peak in all nuclei, increasing in size<sup>3</sup> after  $^{48}\text{Ca}$ . (The IS strength functions of  $^{72,74,76}\text{Ca}$  are multiplied by 0.1 in the figure.) In  $^{76}\text{Ca}$  45 % of the energy-weighted strength is below 10 MeV. The IV strength functions also have increasing low-energy strength at large  $N$ . The small low-energy bump in  $^{50}\text{Ca}$  is produced by SLy4 as well as SkM\*.

We see similar  $N$ -dependence in Ni (see Fig. 11), though after  $^{90}\text{Ni}$  the low-energy IS peak shrinks. The threshold for rapid growth with both Skyrme interactions is the closed-shell nucleus  $^{78}\text{Ni}$ . In Sn, once again, the low-energy IS peak grows with  $N$ , though more smoothly than in the other isotopes (see Fig. 12). In particular, there is apparently no sudden increase at the closed-shell-plus-two nucleus  $^{134}\text{Sn}$ . Recently, Ref. [36] reported a clear IV bump around 10 MeV in that nucleus. The bumps in our calculated spectra do not seem to really set in until higher  $N$ .

The  $1^- W_E$  tell a slightly different story (Figs. 13–18). The partial sums in the IS channel of Sn (Fig. 17) show a noticeable kink at  $N = 82$ , due clearly to an increase in low-energy strength. As remarked above, the increase is not obvious in the strength-function figures. The choice of interaction makes very little difference in the  $W_E$  except in the blank regions (indicating quadrupole deformation) and near the neutron drip line.

According to the analytical argument in the previous subsection, if the IV EWSR depends on the interaction in one multipole, then it should in all multipoles. As Figs. 14, 16, and 18 show, this is indeed the case.

We have not commented on the question of whether protons are involved in the transitions to low-lying states in this channel because the IS and IV operators do not have the same radial dependence. We will address the issue in later when we display transition densities.

---

<sup>3</sup> The low-energy peaks of  $^{42-48}\text{Ca}$  are so sharp because we smooth the strength functions with a smaller width at bound states than in the continuum (see Ref. [28]).

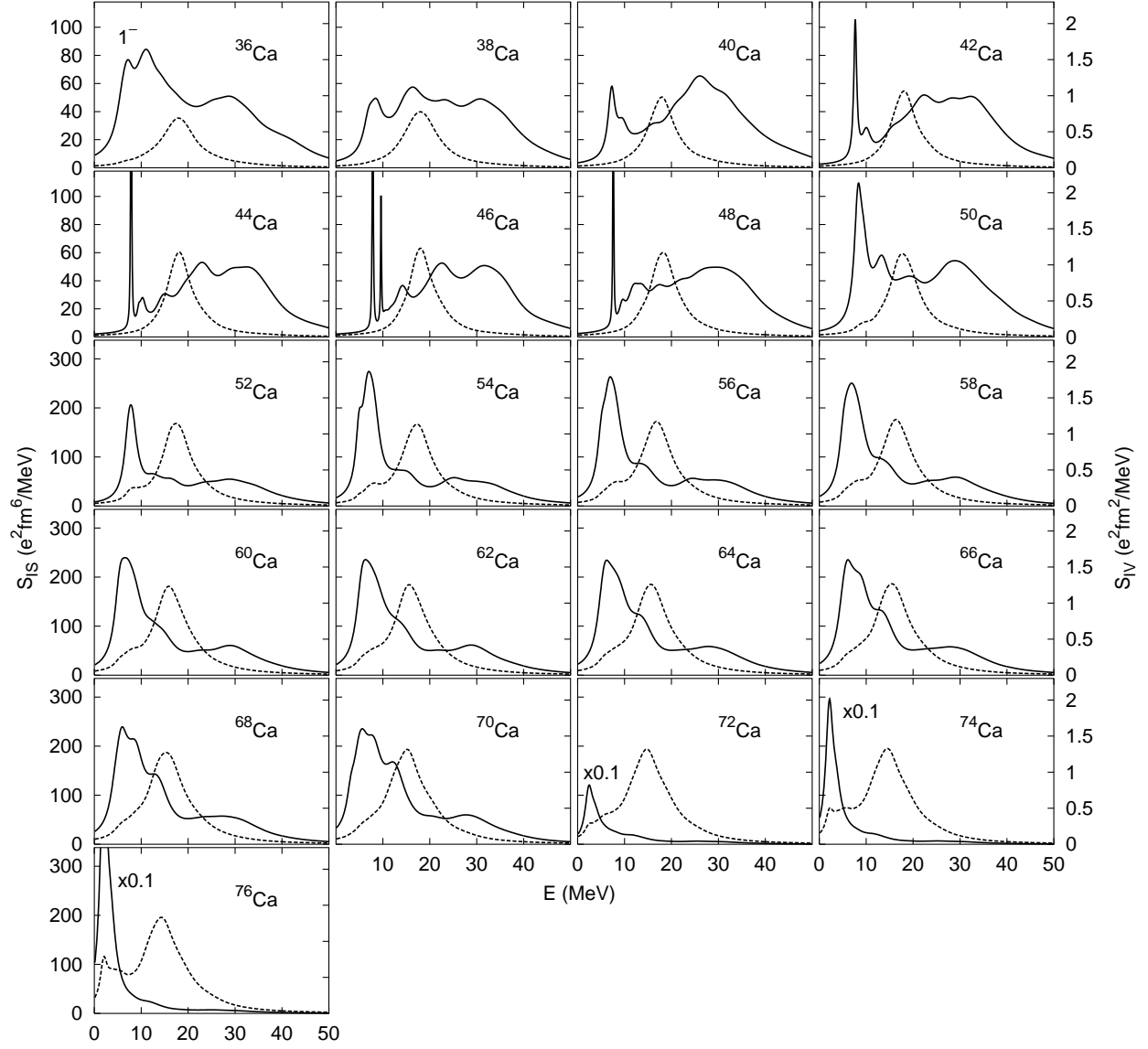


FIG. 10: IS (solid, scale on left) and IV (dashed, scale on right)  $1^-$  strength functions for even Ca isotopes (SkM\*). The IS strength functions in  $^{72,74,76}\text{Ca}$  are reduced by a factor of 10.

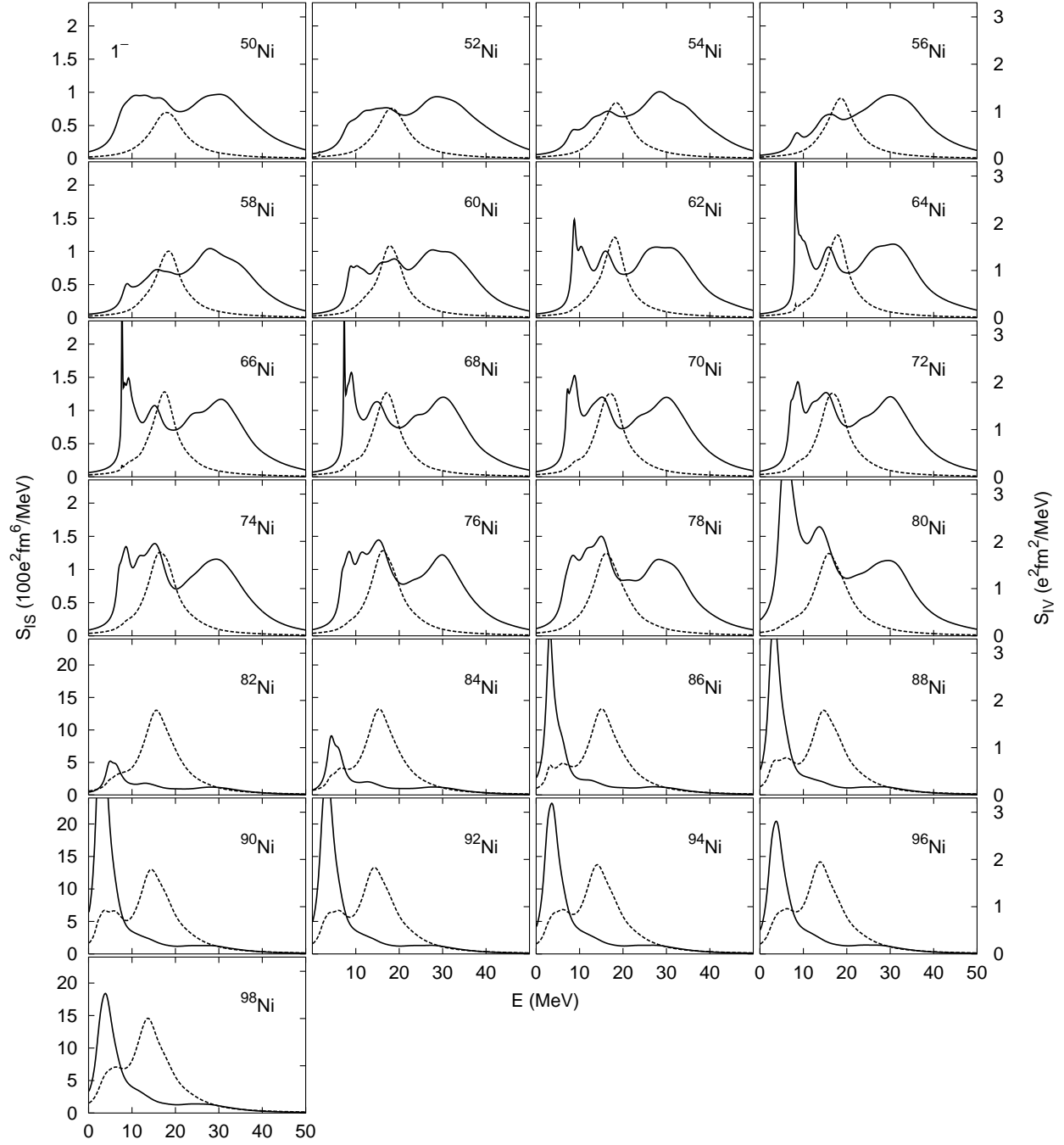


FIG. 11: IS (solid, scale on left) and IV (dashed, scale on right)  $1^-$  strength functions for even Ni isotopes (SkM\*).

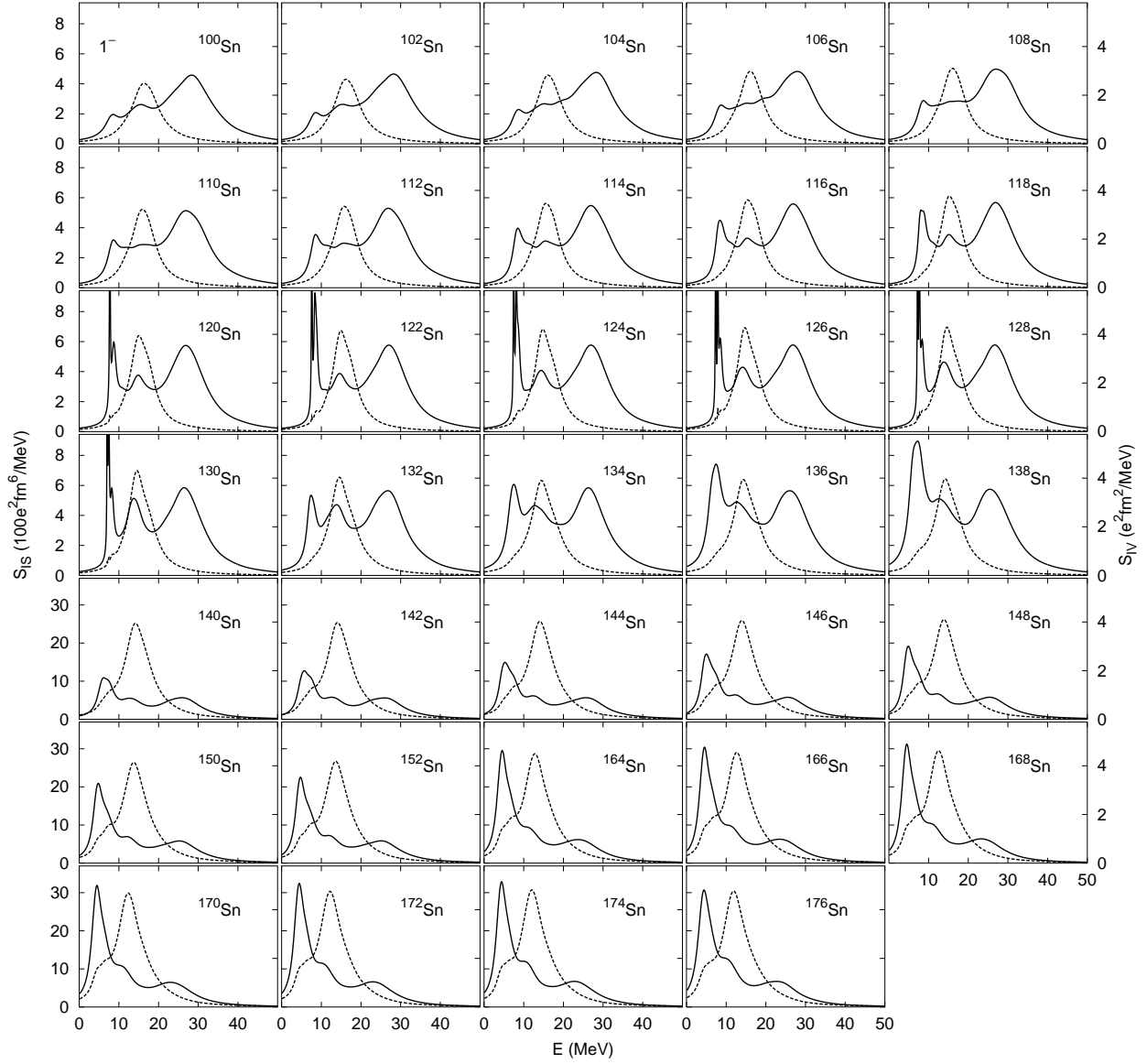


FIG. 12: The same as Fig. 11 but for Sn isotopes.

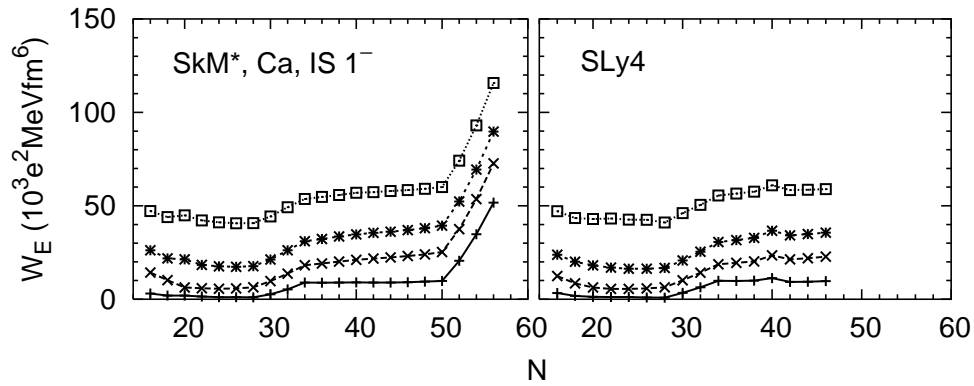


FIG. 13: The same as Fig. 4 but for the  $1^-$  channel.



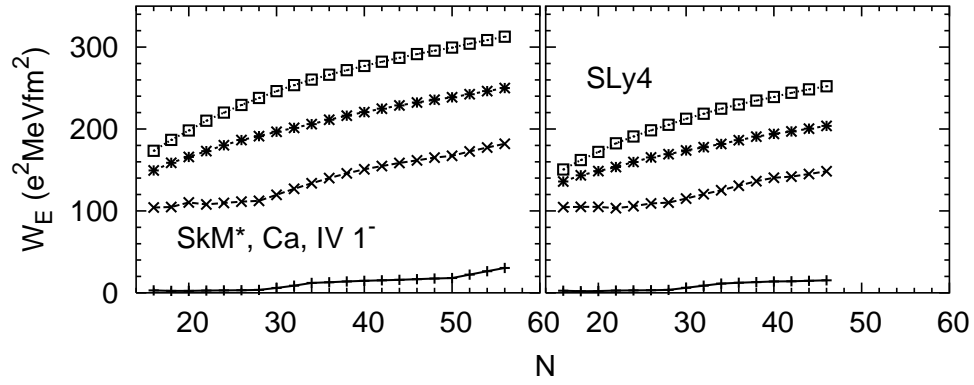


FIG. 14: The same as Fig. 5 but for the  $1^-$  channel.

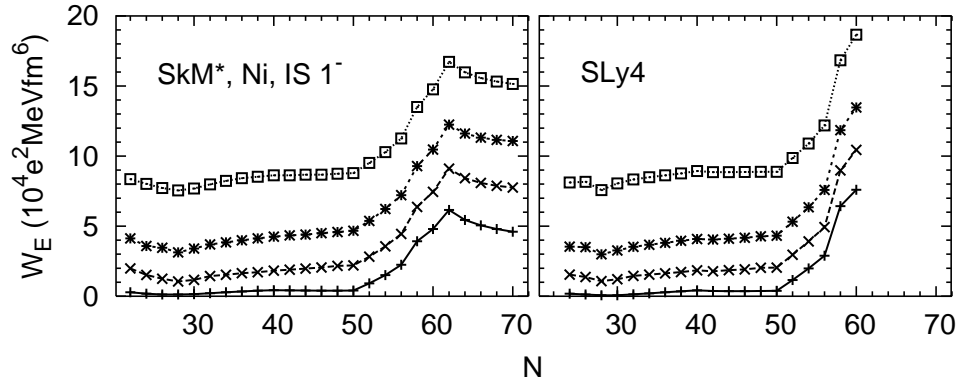


FIG. 15: The same as Fig. 6 but for the  $1^-$  channel.

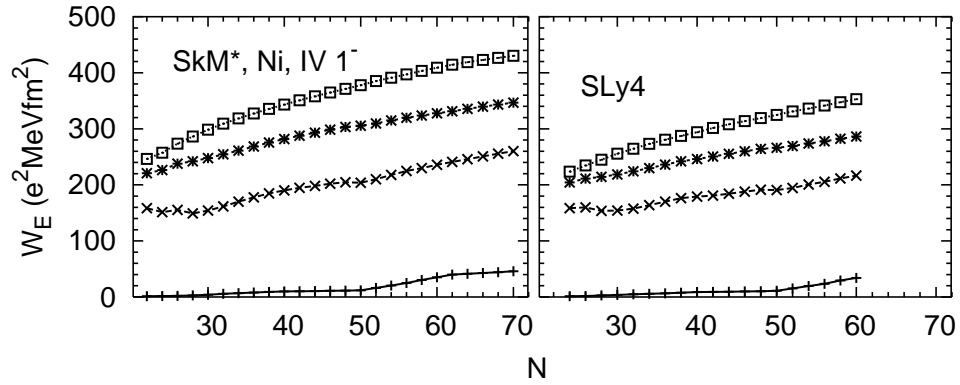


FIG. 16: The same as Fig. 7 but for the  $1^-$  channel.

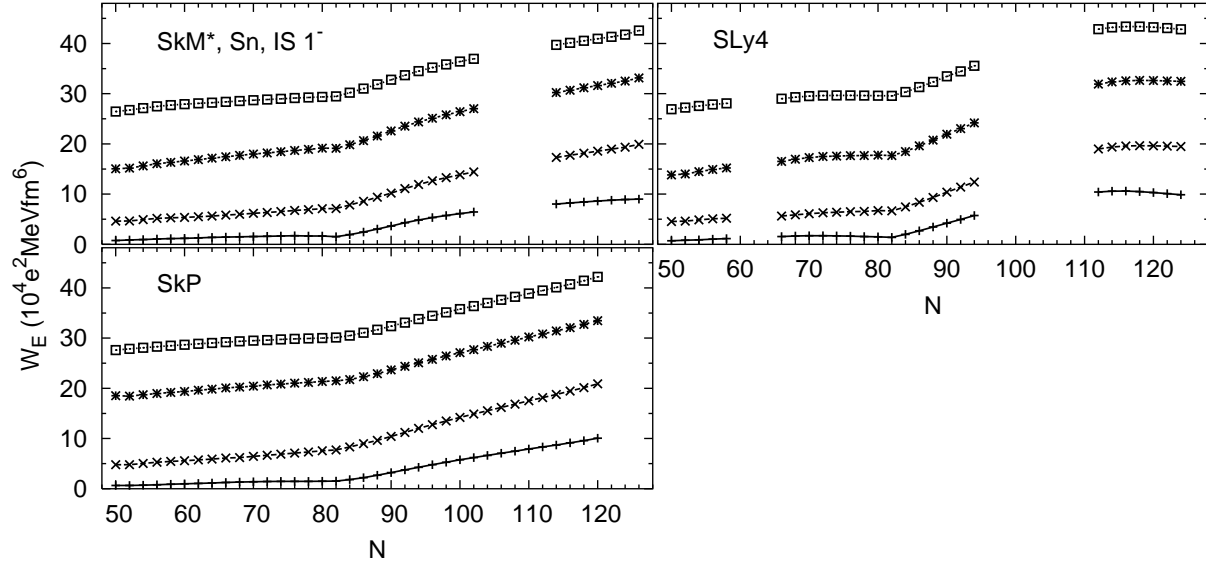


FIG. 17: The same as Fig. 8 but for the  $1^-$  channel.

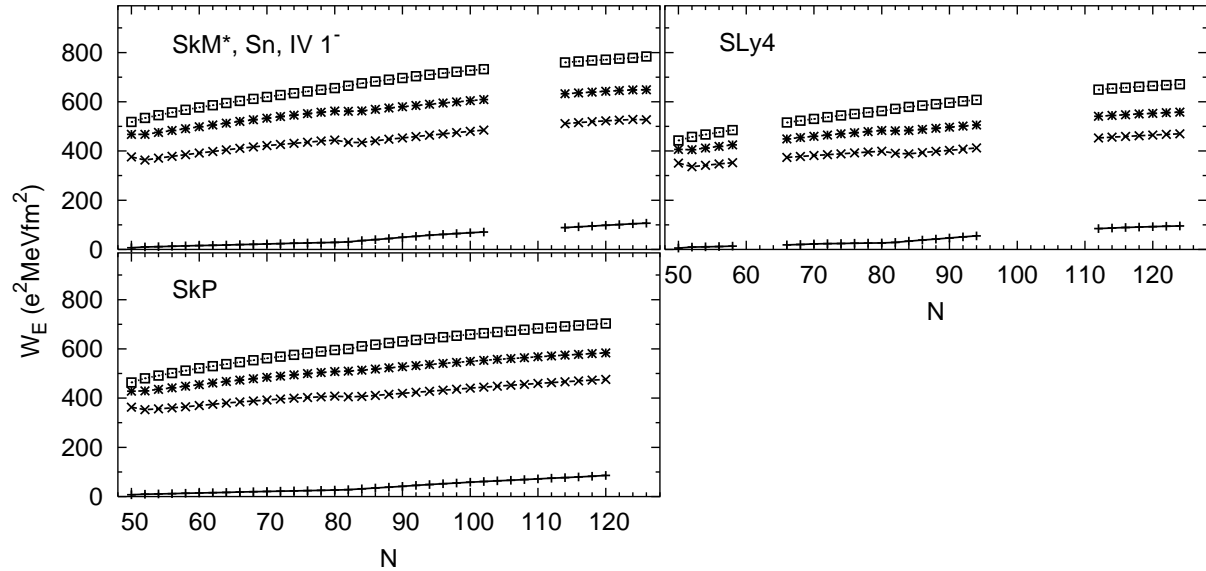


FIG. 18: The same as Fig. 9 but for  $1^-$  channel.

### C. The $2^+$ channels

The strength functions in the  $2^+$  channels are qualitatively different from those in the lower-multipole channels. In Ca, for example (Fig. 19), all isotopes<sup>4</sup> except  $N = 40$  have considerable low-energy strength, in many instances because of sharp quadrupole vibrations. The low-energy strength grows with  $N$ , but unlike in the  $0^+$  channel, both neutrons and protons are involved in the transitions to these states, even near the drip line, because IS and IV distributions do not coincide. This is so for all Skyrme interactions. In fact the IS strength at low energies is much larger than the IV strength in all isotopes except  $^{76}\text{Ca}$ . Even there, the IS strength to the low-energy peak with SkM\* is  $256 e^2\text{fm}^4$  and the IV strength only  $136 e^2\text{fm}^4$ .

The  $2^+$  strength functions in Ni (Fig. 20) are similar, though with two differences: all the nickel isotopes have low-energy peaks, and for  $^{90-98}\text{Ni}$  the IV peak is at a different energy than the IS peak. The lowest-lying peak seems to be nearly pure IS, like the familiar surface-quadrupole vibrations in stable nuclei. In the next section we will discuss the extent to which the states near the neutron-drip line display the same vibrational features we observe near stability.

SLy4 puts the drip line at  $^{88}\text{Ni}$ , much closer to stability, and in isotopes close to  $^{88}\text{Ni}$  puts the IS and IV peaks at about the same location. In the lighter ( $A \geq 80$ ) Ni isotopes, the lowest peak always has a little bit of IV strength mixed with the IS strength, as with SkM\*. In  $^{80}\text{Ni}$  (SkM\*), the IV strength in the peak at 400 keV is 5 % of the IS strength.

Things are quite similar in Sn (Fig. 21); for  $^{134-170}\text{Sn}$  the lowest-energy peak has both IS and the IV components but in  $^{172-176}\text{Sn}$  it has no IV component. The other interactions give the same results near the neutron drip line, indicating again that proton excitations are important in these modes everywhere.

The predictions for  $W_E$  in Ca (Fig. 22) show that SLy4 evinces slightly more of a closed shell (a small kink in the 10-MeV curve) at  $N = 40$  than does SkM\*, while showing less of a shell effect at  $N = 28$  (no small kink in the 20-MeV curve). As was the case in the  $0^+$  and  $1^-$  channels, the IV  $W_E$  (Fig. 23) depends on the interaction.

Similar differences in shell-strength among the Skyrme interactions are apparent in the Ni and Sn  $W_E$  curves for the IS channel (Figs. 24 and 26), while the difference is not obvious in the IV channels (Figs. 25 and 27). The IS  $W_E$  for Sn (Fig. 26) indicate that SkP has more low-energy strength ( $N > 82$ ) than the other parameter sets. The IV curves in Sn show interaction differences similar to those in the  $1^-$  channel.

---

<sup>4</sup> Reference [15] calculates the  $2^+$  strength functions of  $^{60}\text{Ca}$  without low-energy peaks; we do not know the reasons for the difference between that calculation and ours.

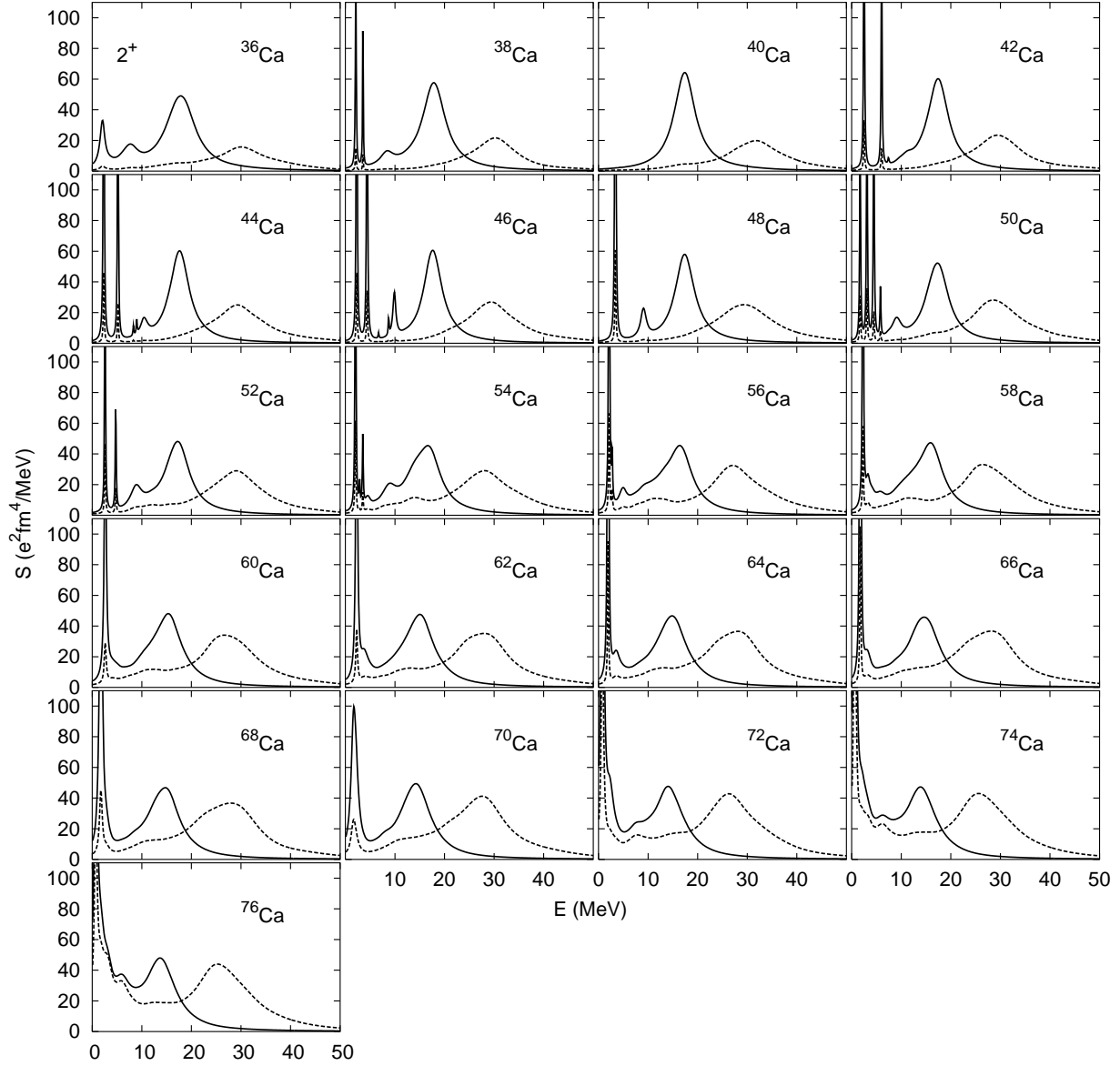


FIG. 19: IS (solid) and IV (dashed)  $2^+$  strength functions in even Ca isotopes (SkM\*).

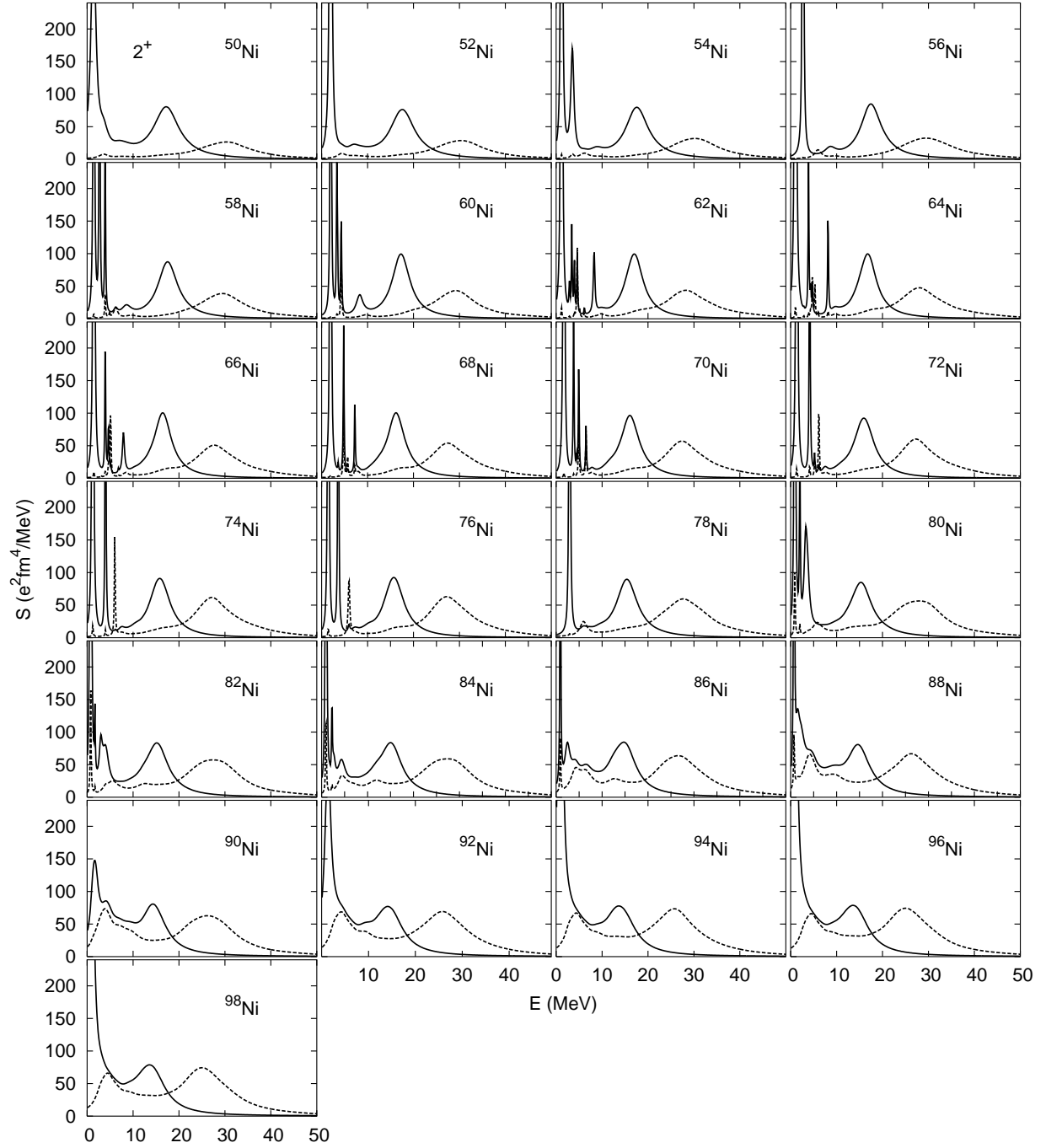


FIG. 20: The same as Fig. 19 but for Ni isotopes.

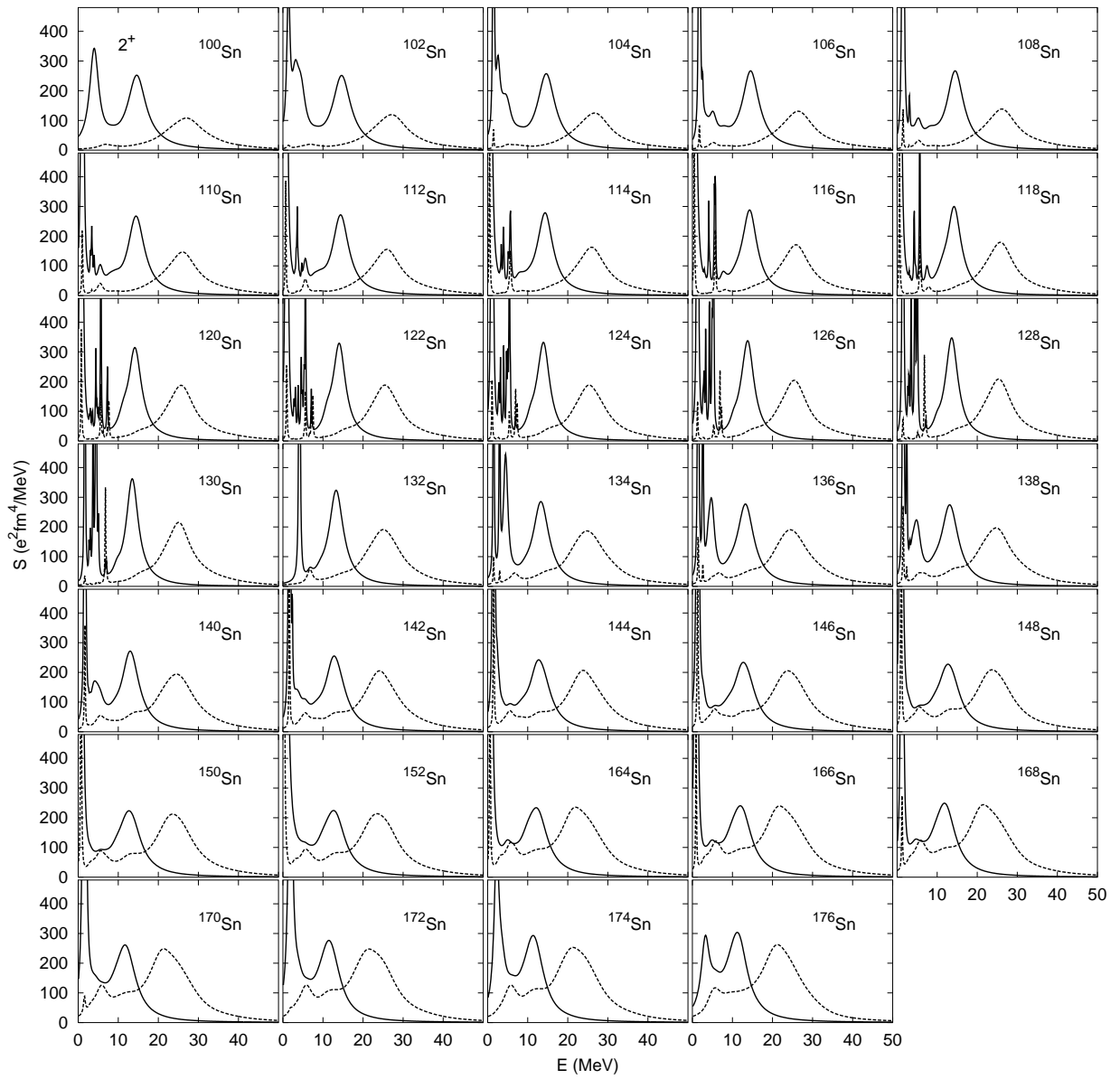


FIG. 21: The same as Fig. 19 but for Sn isotopes.

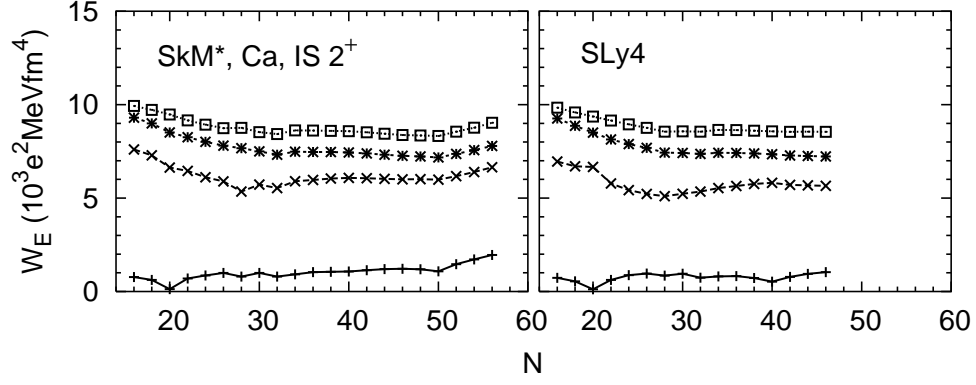


FIG. 22: The same as Fig. 4 but for the  $2^+$  channel.

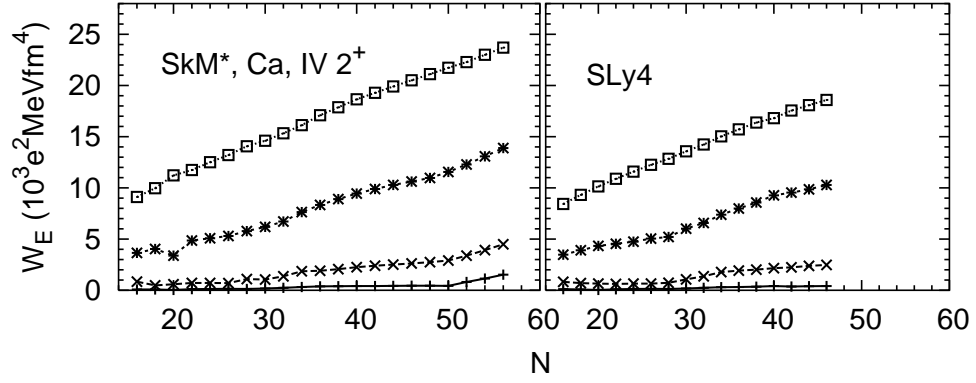


FIG. 23: The same as Fig. 5 but for the  $2^+$  channel.

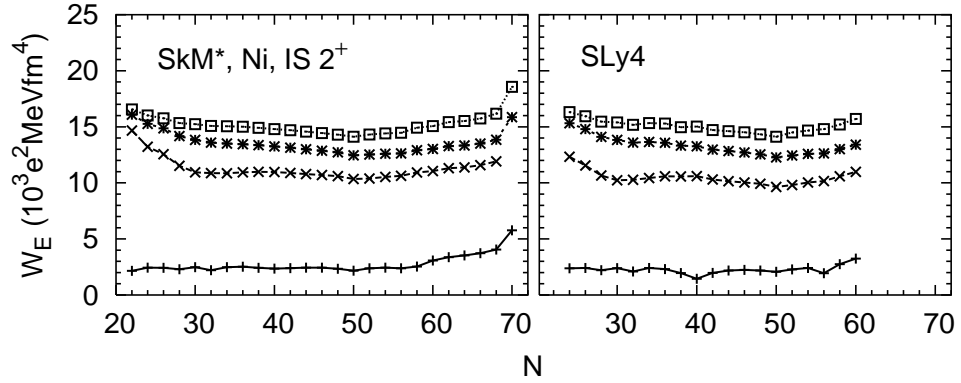


FIG. 24: The same as Fig. 6 but for the  $2^+$  channel.

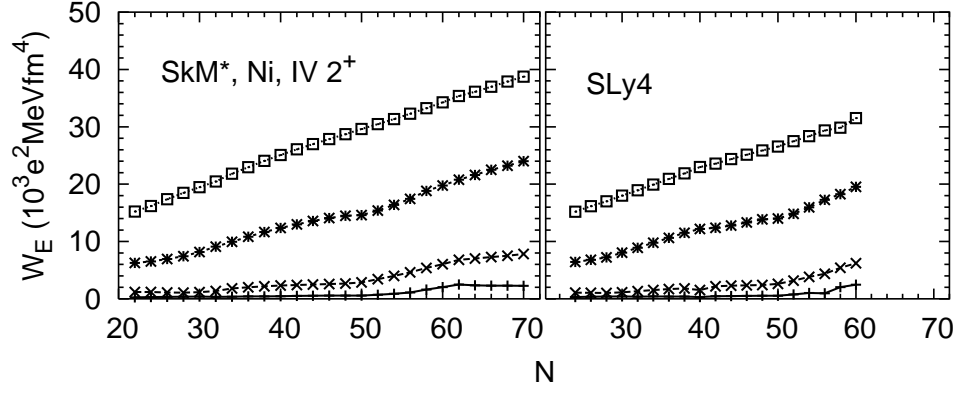


FIG. 25: The same as Fig. 7 but for the  $2^+$  channel.

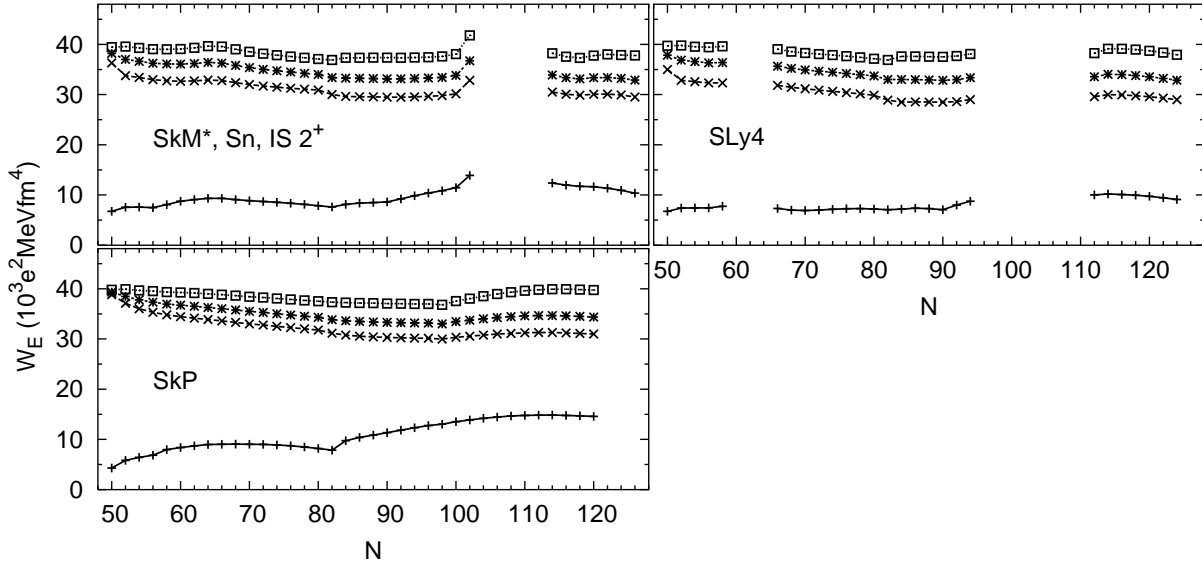


FIG. 26: The same as Fig. 8 but for the  $2^+$  channel.



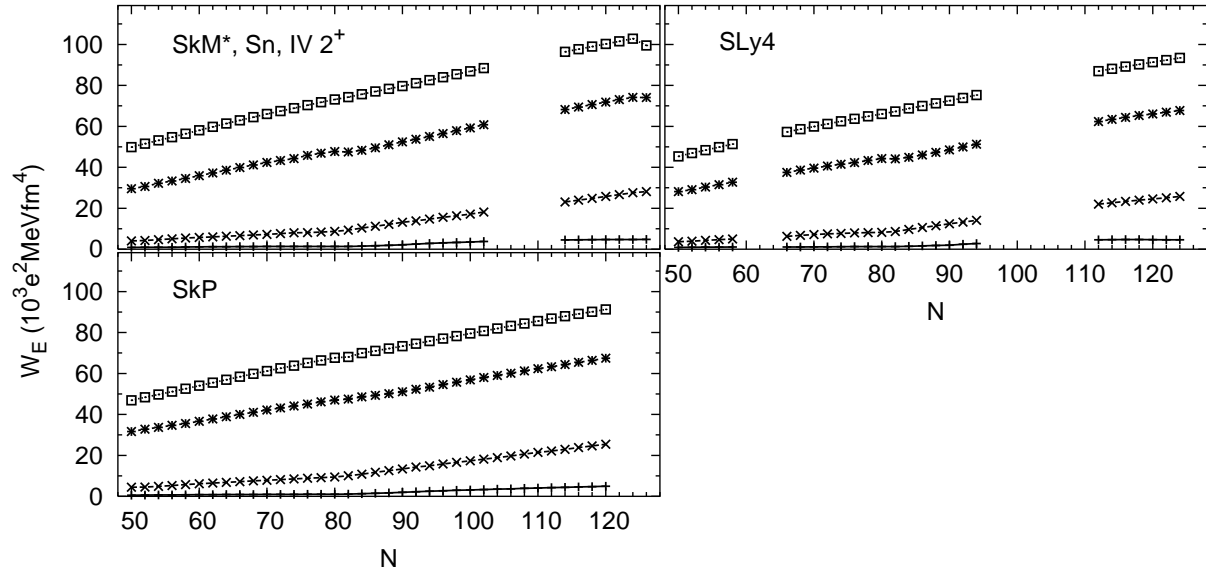


FIG. 27: The same as Fig. 9 but for  $2^+$  channel.

## IV. TRANSITION DENSITIES

Giant resonances lie in the continuum and their  $N$ -dependence is therefore smooth. The low-energy peaks, on the other hand, can vary dramatically with  $N$ , especially near the drip line. In this section, to learn more about their collectivity and  $N$  dependence, we examine transition densities to representative low-lying states.

The transition density  $\rho_{\text{tr}}^q(\mathbf{r}; k)$  is defined in the Appendix. Here we focus on the radial transition density

$$\rho_{\text{tr}}^q(r; k) = r^2 \int d\Omega Y_{J_k M_k}(\Omega) \rho_{\text{tr}}^q(\mathbf{r}; k). \quad (12)$$

The transition amplitude depends on this quantity through the relation

$$\langle k | \hat{F}_{JM} | 0 \rangle = \int dr \sum_{q=p,n} f^q(r) \rho_{\text{tr}}^q(r; k), \quad (13)$$

where  $f^q(r)$  is the radial part of the multipole operator  $\hat{F}_{JM}$ . The radial transition density therefore specifies the radius at which the strength is large or small. The transition density, as Eq. (A.2) shows, is proportional to the product of particle and hole wave functions and so is localized as long as all hole states are localized, i.e. as long as the ground state is bound. In this section, as before, we will be using SkM\* unless we state otherwise.

### A. The $0^+$ channels

Figure 28 shows the transition densities to 4 states below the giant resonances in  $^{36}\text{Ca}$  with large strengths (the energies label the results of the QRPA calculation before smoothing). Proton excitations are important, particularly because of the factor  $r^2$  in the  $0^+$  transition operator. The rms radii of the protons and neutrons in the ground state are 3.40 and 3.19 fm. The important part for the strength comes from outside the rms radius.

This is not true of the giant resonances. Figure 29 shows transition densities in the peaks of the giant resonances of  $^{36}\text{Ca}$ . The upper two panels represent the IS giant resonance, and as is expected the protons and neutrons have similar transition densities. In the lower panels, corresponding to the IV giant resonance, the two densities are out of phase. The peaks of the proton transition densities are closer to the center of the nucleus than those of the lower-energy states, particularly in the IS channel.

We saw that a small bump appeared after magic numbers in neutron-rich nuclei. In Ca, the relevant isotope is  $^{50}\text{Ca}$ . (Fig. 30) shows that the excitation is created entirely by neutrons. But the state is not at all collective. The largest two-quasiparticle component in the QRPA wave function is  $\nu 3p_{3/2}(\mathcal{E} = 9.175 \text{ MeV}, \bar{v}_\mu^2 = 6.0 \times 10^{-4}) \otimes \nu 2p_{3/2}(\mathcal{E} = 0.880 \text{ MeV}, \bar{v}_\mu^2 = 0.488)$ , where  $\mathcal{E}$  is the quasiparticle energy in the HFB quasiparticle basis and  $\bar{v}_\mu^2$  is the diagonal ground-state occupation probability (norm of the lower component of the quasiparticle wave function). The radial quantum numbers are assigned in order of  $\mathcal{E}$  ( $-\mathcal{E}$  for those having  $\bar{v}_\mu^2 > 0.5$ ).  $\bar{X}_{\mu\nu}(\bar{Y}_{\mu\nu})$  is the forward (backward) amplitude of the QRPA solution.

The squared amplitude  $\bar{X}_{\mu\nu}^2 - \bar{Y}_{\mu\nu}^2$  of the  $\nu 3p_{3/2} \otimes \nu 2p_{3/2}$  component is 0.980. The component corresponds to the excitation of a neutron from a  $p_{3/2}$  orbit near the Fermi surface to another  $p_{3/2}$  orbit about 9 MeV above. The first orbit is strongly affected by pairing correlations. The two-quasiparticle energy is 10.055 MeV, and the energy of the excited state

itself is 10.005 MeV; the excitation is clearly almost unaffected by the residual interaction. Yet this nearly pure two-quasiparticle state, because the neutron transition density has such a long tail, carries 5 % of the total IS transition strength. Furthermore, protons contribute essentially nothing to the transition; the maximum of the  $\bar{X}_{\mu\nu}^2 - \bar{Y}_{\mu\nu}^2$  for protons is  $0.3 \times 10^{-4}$ . This remarkable situation — dominance by a single two-neutron-quasiparticle configuration with very large strength, occurs in the  $0^+$  channel repeatedly.

Take, for example, the drip-line nucleus  $^{76}\text{Ca}$ . Two low-lying states, at  $E = 2.391$  and  $2.995$  MeV, together account for 25.8 % of the total IS strength and 10.2 % of the EWSR. Transition densities, shown in Fig. 31, are again dominated by neutrons, with outer peaks at 9–11 fm. The rms ground-state radii are 3.738 fm for protons and 4.615 fm for neutrons, so the highest (inner) peaks of  $\rho_{\text{tr}}(r; k)$  are close to the neutron rms radius. The main component of the excited state with  $E = 2.391$  MeV, with a squared amplitude of 0.807, is  $\nu 3s_{1/2}(\mathcal{E} = 0.355 \text{ MeV}, \bar{v}_\mu^2 = 0.645) \otimes \nu 4s_{1/2}(\mathcal{E} = 2.092 \text{ MeV}, \bar{v}_\mu^2 = 0.012)$ . The main component of the state at  $E = 2.995$  MeV, with a squared amplitude of 0.930, is  $\nu 2d_{5/2}(\mathcal{E} = 0.617 \text{ MeV}, \bar{v}_\mu^2 = 0.78) \otimes \nu 3d_{5/2}(\mathcal{E} = 2.457 \text{ MeV}, \bar{v}_\mu^2 = 6.1 \times 10^{-3})$ . Like before, these are nearly pure two-neutron-quasiparticle states with long tails in their product.

Turning now to Ni near the closed  $N = 50$  shell, we see that  $^{80}\text{Ni}$  has a small bump around 5 MeV, while  $^{78}\text{Ni}$  does not (Fig. 2). The transition density in Fig. 32 again shows neutron dominance. This excited state has 2.8 % of the total IS strength, and its main component is  $\nu 2d_{5/2}(\mathcal{E} = 0.738 \text{ MeV}, \bar{v}_\mu^2 = 0.31) \otimes \nu 3d_{5/2}(\mathcal{E} = 5.088 \text{ MeV}, \bar{v}_\mu^2 = 7.1 \times 10^{-4})$ , with  $\bar{X}_{\mu\nu}^2 - \bar{Y}_{\mu\nu}^2 = 0.761$ . At the drip-line nucleus  $^{98}\text{Ni}$ , the main component of the excited state at  $E = 3.452$  MeV, which is one of the states forming a low-energy bump, is  $\{\nu 3d_{3/2}(\mathcal{E} = 1.799 \text{ MeV}, \bar{v}_\mu^2 = 0.359)\}^2$ ; it has  $\bar{X}_{\mu\nu}^2 - \bar{Y}_{\mu\nu}^2 = 0.818$ .

In Sn the nucleus just past the closed neutron shell is  $^{134}\text{Sn}$ . Here, as we noted earlier, a new bump is not visible (Fig. 3), until  $^{136}\text{Sn}$ . We show the transition density to the corresponding state in Fig. 33. The excitation's main component is  $\nu 2f_{7/2}(\mathcal{E} = 0.950 \text{ MeV}, \bar{v}_\mu^2 = 0.44) \otimes \nu 3f_{7/2}(\mathcal{E} = 6.302 \text{ MeV}, \bar{v}_\mu^2 = 6.2 \times 10^{-4})$ , with  $\bar{X}_{\mu\nu}^2 - \bar{Y}_{\mu\nu}^2 = 0.902$ .  $\mathcal{E} = 0.950$  MeV is the smallest neutron quasiparticle energy of the HFB calculation. Figure 34 shows the transition densities to three states in the low-energy bump in  $^{176}\text{Sn}$ . The behavior is similar to that in the drip-line Ca and Ni nuclei.

We turn finally to the dependence of the transition densities on the Skyrme interaction. Figure 35 shows, unsurprisingly by now, that SkM\* and SLy4 give similar transition densities to states below the giant resonances in  $^{36}\text{Ca}$ . We show transition densities for some giant-resonance states in Fig. 36. The IS/IV character of those states is clear.

Next we compare predictions for  $^{50}\text{Ca}$ . Figure 37 shows the SLy4 transition densities to the states in the small bump in the low-energy continuum. The bump emerges there with both interactions.  $^{66}\text{Ca}$  is the neutron-drip-line nucleus obtained with SLy4; Figure 38 displays the strength functions in that nucleus. Apparently they are similar not to those of the SkM\* drip-line nucleus  $^{76}\text{Ca}$  but rather to those of the SKM\*  $^{66}\text{Ca}$  (see Fig. 1). Clearly the quantum numbers of the quasiparticle orbits involved in the transition affect the transition density much more than the chemical potential.

Figures 39 (SLy4) and 40 (SkM\*) show the transition densities to the excited states in the shoulder at about 9 MeV in  $^{66}\text{Ca}$ . The positions of the outer neutron peak are nearly the same in both, but the neutron transition densities for  $r < 4$  fm have some differences. The proton transition density is small except in the right panel of Fig. 40. The tails of the transition densities are quite different from those in Fig. 31, for the nucleus with 10 more neutrons. The two-quasiparticle components with the largest amplitude involve either

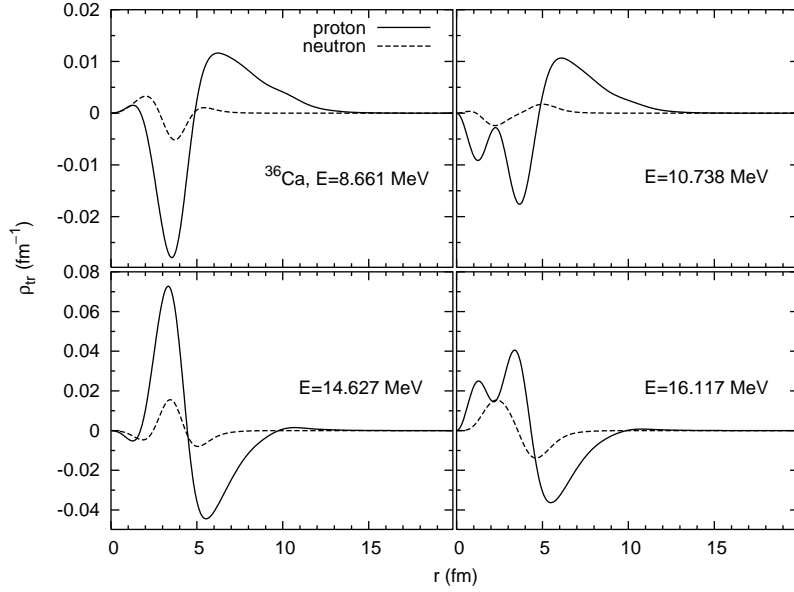


FIG. 28: Proton and neutron transition densities to the four states in  $^{36}\text{Ca}$  in the peaks of the strength function ( $E < 17$  MeV) in Fig. 1.

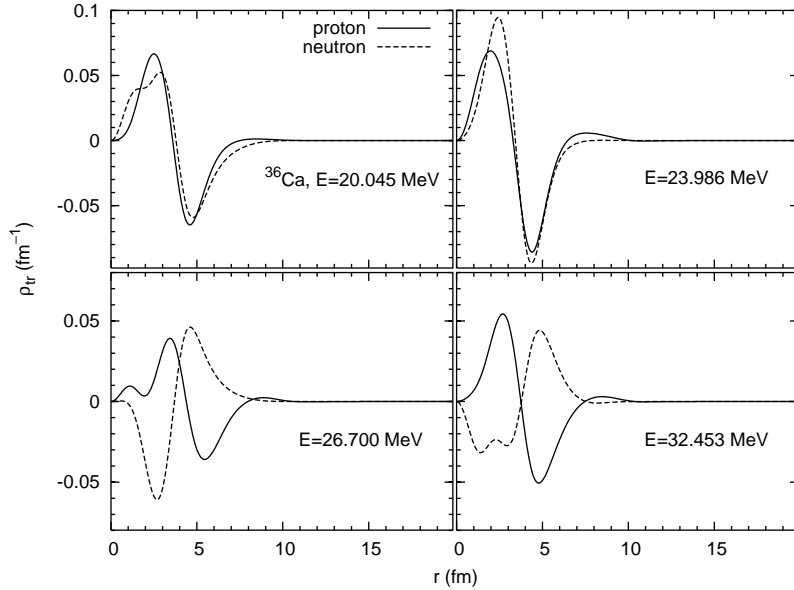


FIG. 29: The same as Fig. 28 but for the giant resonances. The states in the upper panels correspond to the peaks of the IS giant resonance, and in the lower to the IV giant resonance.

neutron  $g_{9/2}$ 's or  $p_{3/2}$ 's, depending on the state and interaction, and the largest amplitude itself ranges from 0.5 to 0.99.

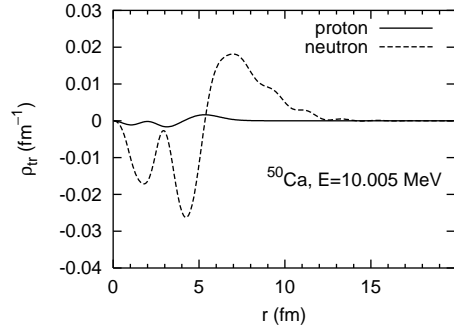


FIG. 30: Transition densities to the excited state in the small low-energy bump in the  $0^+$  strength function of  $^{50}\text{Ca}$ .

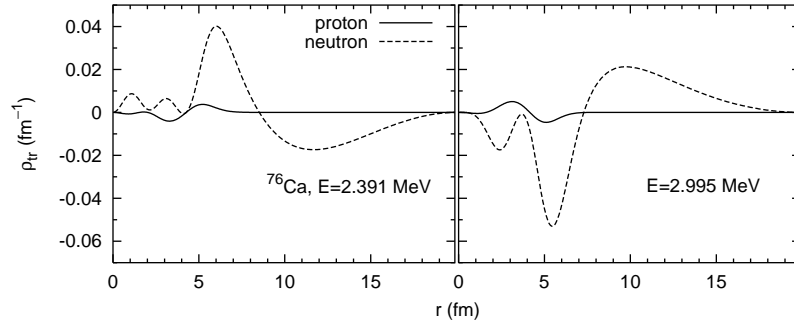


FIG. 31: Transition densities to the two excited states in the low-energy peak in the  $0^+$  strength functions of  $^{76}\text{Ca}$ .

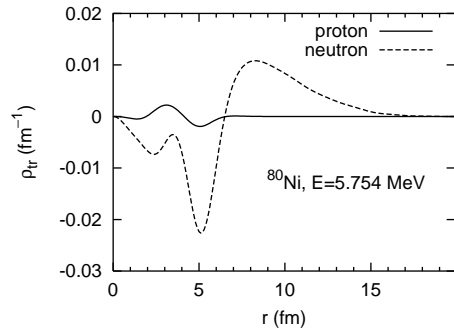


FIG. 32: Transition densities to the excited state in the small low-energy bump in the  $0^+$  strength function of  $^{80}\text{Ni}$ .

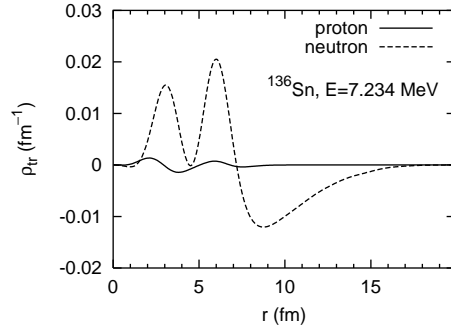


FIG. 33: Transition densities to the excited state in a small bump in the  $0^+$  strength function of  $^{136}\text{Sn}$ .

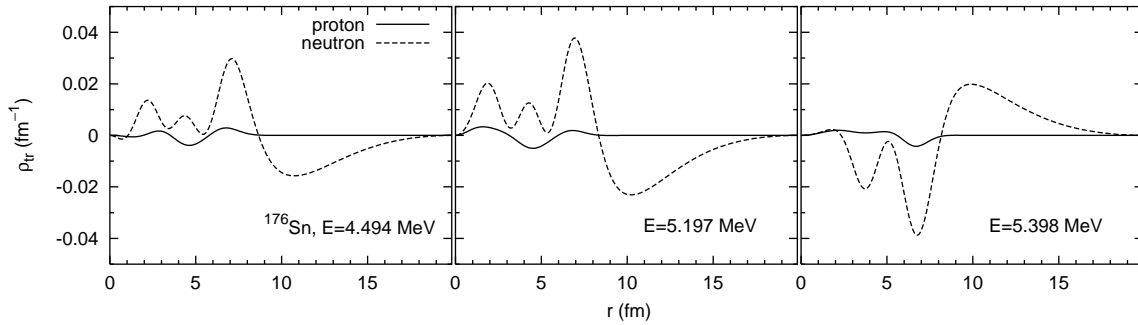


FIG. 34: Transition densities to the excited state in a small bump in the  $0^+$  strength function of  $^{176}\text{Sn}$ .

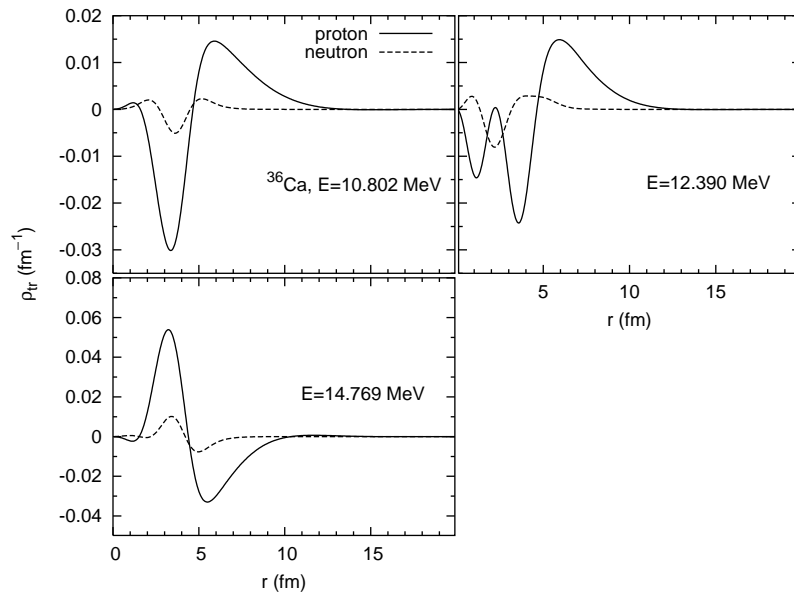


FIG. 35: Transition densities to the  $0^+$  excited states below the giant resonances in  $^{36}\text{Ca}$  with relatively large strength (SLy4).

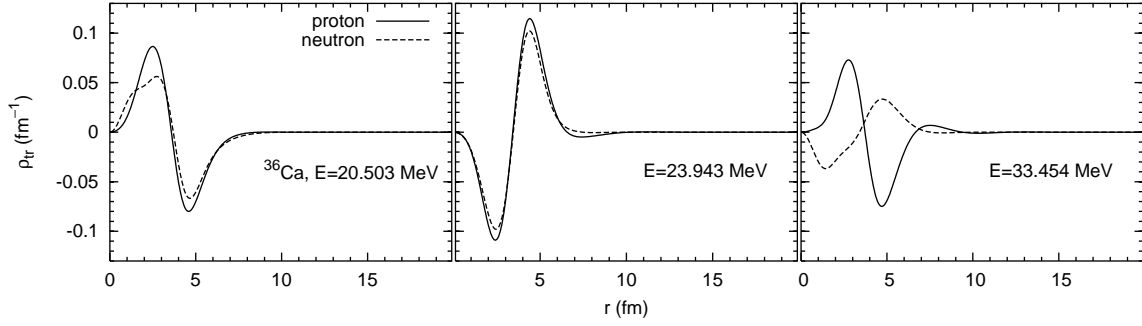


FIG. 36: Transition densities to the  $0^+$  excited states of  $^{36}\text{Ca}$  in the giant resonances (SLy4).

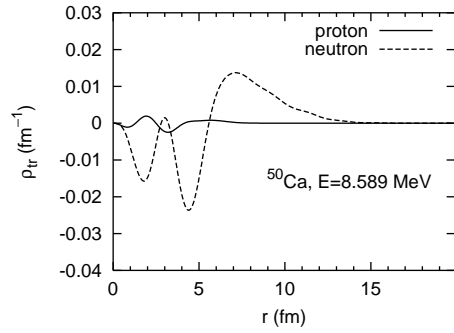


FIG. 37: Transition densities to the  $0^+$  excited states of  $^{50}\text{Ca}$  in a small bump at low-energy (SLy4).

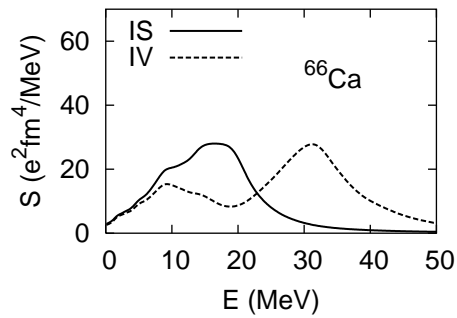


FIG. 38:  $0^+$  strength functions of  $^{66}\text{Ca}$  (SLy4).

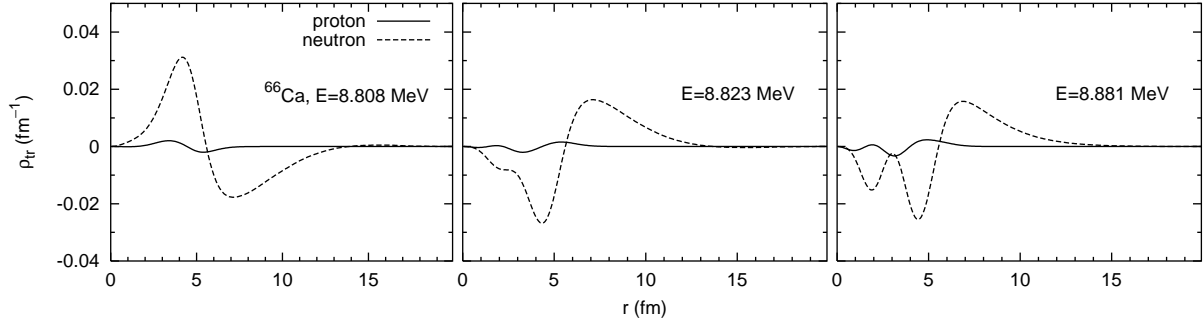


FIG. 39: Transition densities to the excited states in the low-energy shoulder (IS) or peak (IV) around  $E = 9$  MeV of the strength function of Fig. 38 (SLy4).

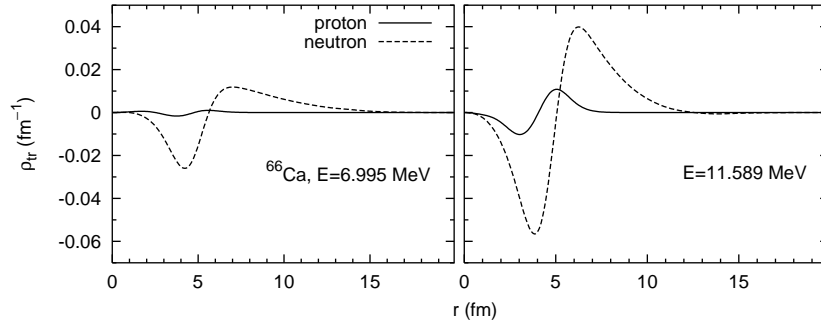


FIG. 40: Transition densities to the excited states in the low-energy shoulders around  $E = 9$  MeV and 11 MeV in the  $0^+$  strength function of  $^{66}\text{Ca}$  (SkM\*).



## B. The $1^-$ channels

As we have just seen, the large neutron tails in the transition density are responsible for enhanced low-lying strength near the drip line. The robust enhancement of low-lying IS  $1^-$  strength is due in large part to the factor  $r^3$ , which emphasizes large radii, in the transition operator.

One stark difference between these transition densities and those of the  $0^+$  channel is the role played by protons, which is non-negligible here. Figure 41 shows the transition densities of two states in the low-lying IS peak in  $^{50}\text{Ca}$ . Protons and neutrons contribute coherently. The component of the state at  $E = 8.228$  MeV with the largest amplitude is  $\nu 2p_{3/2}(\mathcal{E} = 0.880$  MeV,  $\bar{v}_\mu^2 = 0.488) \otimes \nu 1d_{3/2}(\mathcal{E} = 8.219$  MeV,  $\bar{v}_\mu^2 = 0.981)$ . The squared amplitude  $\bar{X}_{\mu\nu}^2 - \bar{Y}_{\mu\nu}^2$  is only 0.36. Two other configurations,  $\nu 3s_{1/2} \otimes \nu 2p_{3/2}$  and  $\pi 2p_{3/2} \otimes \pi 1d_{3/2}$  have  $\bar{X}_{\mu\nu}^2 - \bar{Y}_{\mu\nu}^2 = 0.20$  and 0.12, not much smaller. And since the two-quasiparticle energy of the largest component is 9.099 MeV, the excited state gains more correlation energy than those in the  $0^+$  channel.

The proton contributions remain even at the neutron drip line. Figure 42 shows the transition densities to 3 excited states in the large low-energy IS peak in  $^{76}\text{Ca}$  (Fig. 10). These states have IS strengths  $9227 e^2\text{fm}^6$  ( $E = 1.931$  MeV),  $3219 e^2\text{fm}^6$  ( $E = 2.199$  MeV), and  $4856 e^2\text{fm}^6$  ( $E = 3.501$  MeV), representing 42 %, 15 %, and 22 % of the total strength. While protons play no role for  $r > 6$  fm, they are active around  $r = 5$  fm. The main difference between these states and those of  $^{50}\text{Ca}$  is that here the neutrons both extend much further out and contribute more inside the nucleus. It is the tail that is mainly responsible for the increased strength.

Interestingly, the states in  $^{76}\text{Ca}$  are mainly of two-quasiparticle character even though there is a coherent proton contribution. The component in the state at  $E = 1.931$  MeV with the largest amplitude ( $\bar{X}_{\mu\nu}^2 - \bar{Y}_{\mu\nu}^2 = 0.914$ ) is  $\nu 3s_{1/2}(\mathcal{E} = 0.355$  MeV,  $\bar{v}_\mu^2 = 0.645) \otimes \nu 3p_{3/2}(\mathcal{E} = 1.582$  MeV,  $\bar{v}_\mu^2 = 0.592 \times 10^{-3})$ . In the state at  $E = 2.199$  MeV the component with the largest amplitude ( $\bar{X}_{\mu\nu}^2 - \bar{Y}_{\mu\nu}^2 = 0.975$ ) is  $\nu 3p_{3/2} \otimes \nu 2d_{5/2}(\mathcal{E} = 0.618$  MeV,  $\bar{v}_\mu^2 = 0.776)$ , and at  $E = 3.501$  MeV it is  $\nu 2d_{5/2} \otimes \nu 2f_{7/2}(\mathcal{E} = 2.860$  MeV,  $\bar{v}_\mu^2 = 0.1 \times 10^{-3})$ , with  $\bar{X}_{\mu\nu}^2 - \bar{Y}_{\mu\nu}^2 = 0.936$ . The proton two-quasiparticle configuration with the largest amplitude has  $\bar{X}_{\mu\nu}^2 - \bar{Y}_{\mu\nu}^2 = (0.2 - 0.3) \times 10^{-2}$ .

In Ni, a low-energy peak rises suddenly at  $^{80}\text{Ni}$  (Fig. 11). The transition densities of the states in the peak, shown in Fig. 43, are similar to those of the neutron-rich Ca isotopes. The density in  $^{98}\text{Ni}$ , at the drip line, is similar though larger. In Sn there is no sudden increase in the low-energy peak around  $N = 82$  (see Fig. 12). Fig. 44 shows the transition densities to low-energy states in three isotopes around  $N = 82$ . Here the proton contributions stretch to larger radii than in Ca or Ni, even though they are dwarfed by the neutron tails there.

The other Skyrme interactions give very similar results, both in the IS and IV channels and for all three isotope chains.

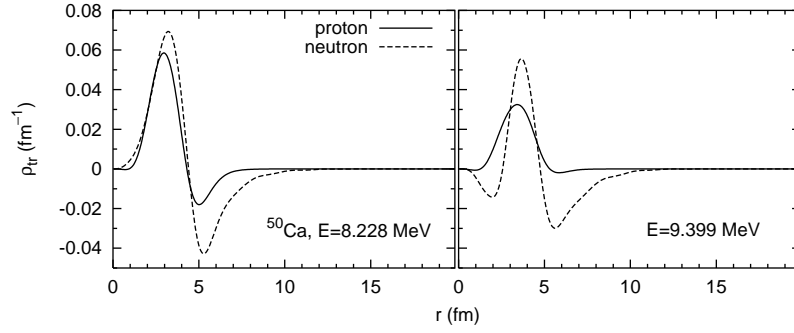


FIG. 41: Transition densities to the excited states in the low-energy peak of the IS  $1^-$  strength function of  $^{50}\text{Ca}$ .

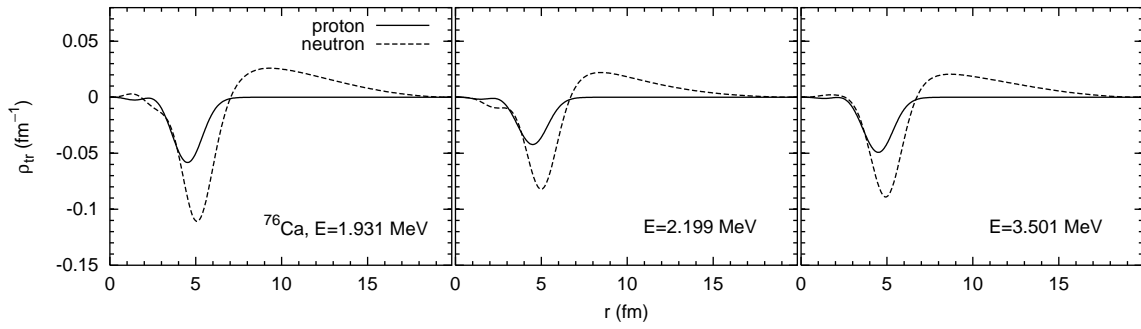


FIG. 42: Transition densities to the excited states in the low-energy peak of the IS  $1^-$  strength function of  $^{76}\text{Ca}$ .

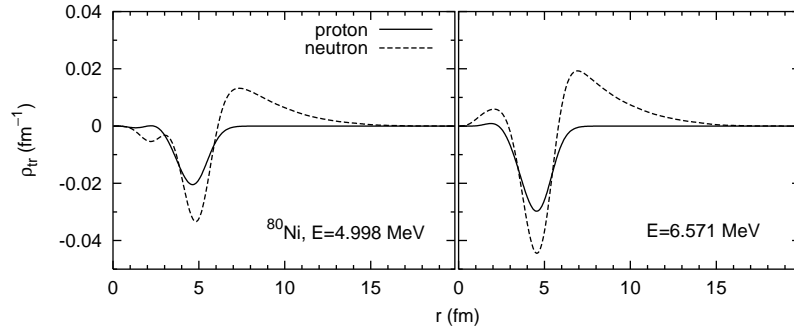


FIG. 43: Transition densities to the excited states in the low-energy peak of the IS  $1^-$  strength function of  $^{80}\text{Ni}$ .

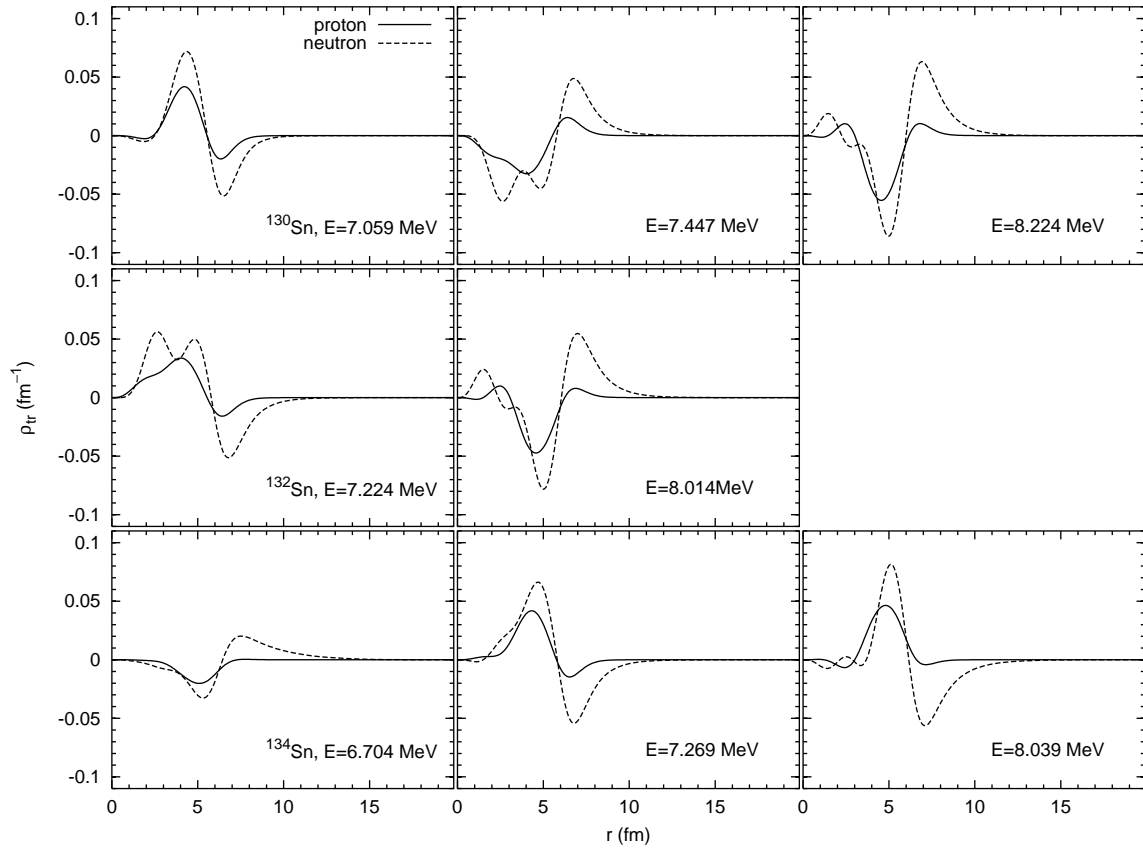


FIG. 44: Transition densities to the excited states in the low-energy peak of the IS  $1^-$  strength function of  $^{130}\text{Sn}$  (upper panels),  $^{132}\text{Sn}$  (middle), and  $^{134}\text{Sn}$  (lower).

### C. The $2^+$ channels

Figures 19–21 showed that at the neutron drip line the IS and IV strength functions in Ni and Sn have distinct low-energy peaks (though the IS strength is always larger, even at the low energy IV peak) while in Ca the peaks coincided. This is true, except in Ni with SLy4<sup>5</sup>, no matter which Skyrme interaction we use. With SkM\*, the IS strength of the large low-energy peak at  $E = 0.096$  MeV in <sup>98</sup>Ni is 92 % of the total strength (8.9 % of the EWSR), and that of the peak at  $E = 0.713$  MeV in <sup>176</sup>Sn is 23 % of the total strength (2.2 % of the EWSR). In Fig. 45 we compare the transition densities of the states in these low-energy peaks with those in <sup>76</sup>Ca. As Fig. 19 suggests, though the protons play a role, the neutrons are proportionately more important in Ca and do not seem to correlate with the protons. In <sup>98</sup>Ni and <sup>176</sup>Sn, by contrast, the neutrons and protons are completely in phase (as they must be if the IV strength is negligible).

The other Skyrme interactions bear out these conclusions, though in the SLy4 calculation of the drip-line Ca isotope the ratio of proton transition density to neutron transition density is larger than that with SkM\* (shown in the left panel of Fig. 45). In all nuclei near the neutron drip line, the states in low-energy peaks are mostly above neutron-emission threshold, yet the neutron tails cut off at much smaller radii than to those in the  $0^+$  and  $1^-$  channels. In addition, the transition densities in those other channels generally have a node at about  $r = 5$  fm, while the  $2^+$  transition densities show no such feature.

We put off for just a moment the obvious question of whether these low-lying IS peaks are familiar quadrupole vibrations and turn briefly to the IV channel. Figure 46 shows the transition densities to states in the low-energy IV strength-function peak in <sup>176</sup>Sn and <sup>98</sup>Ni. The states in <sup>176</sup>Sn display remarkably IS character, despite being at the peak of the IV distribution. The fact that the IV distribution peaks there is a little misleading because the IS strength is still considerably larger, even though it is larger still at lower energies. We get some IV strength because the ratio of the transition density of protons to that of neutrons is not exactly equal to  $Z/N$  (see Eq. (3)).

Returning to the IS strength, we note, in accord with Fig. 45, that the transitions appear more collective in the Ni and Sn drip-line isotopes than in that of Ca. The component with the largest amplitude ( $\bar{X}_{\mu\nu}^2 - \bar{Y}_{\mu\nu}^2 = 0.81$ ) in the state at  $E = 0.713$  MeV of <sup>76</sup>Ca is  $\nu 3s_{1/2}(\mathcal{E} = 0.355$  MeV,  $\bar{v}_\mu^2 = 0.65) \otimes \nu 2d_{5/2}(\mathcal{E} = 0.618$  MeV,  $\bar{v}_\mu^2 = 0.78)$ , and that with the second largest ( $\bar{X}_{\mu\nu}^2 - \bar{Y}_{\mu\nu}^2 = 0.16$ ) is  $\{\nu 2d_{5/2}\}^2$ . This is still a predominantly single two-quasiparticle excitation. By contrast, the components of the state with at  $E = 0.096$  MeV in <sup>98</sup>Ni with the largest amplitudes are

$$\begin{aligned} & \{\nu 1h_{11/2}(\mathcal{E} = 1.415 \text{ MeV}, \bar{v}_\mu^2 = 0.27)\}^2, \bar{X}_{\mu\nu}^2 - \bar{Y}_{\mu\nu}^2 = 0.35, \\ & \{\nu 1g_{7/2}(\mathcal{E} = 1.350 \text{ MeV}, \bar{v}_\mu^2 = 0.59)\}^2, \bar{X}_{\mu\nu}^2 - \bar{Y}_{\mu\nu}^2 = 0.30, \\ & \pi 2p_{3/2}(\mathcal{E} = 2.352 \text{ MeV}, \bar{v}_\mu^2 = 0) \otimes \pi 1f_{7/2}(\mathcal{E} = 2.222 \text{ MeV}, \bar{v}_\mu^2 = 1), \bar{X}_{\mu\nu}^2 - \bar{Y}_{\mu\nu}^2 = 0.12. \end{aligned}$$

While still not very collective, this state is a little more so than its counterpart in Ca. (<sup>98</sup>Ni may be in the spherical-deformed transition region.)

In <sup>176</sup>Sn, the component of the state at  $E = 3.228$  MeV with the largest amplitude is (Fig. 45)  $\nu 2g_{9/2}(\mathcal{E} = 1.477$  MeV,  $\bar{v}_\mu^2 = 0) \otimes \nu 1i_{13/2}(\mathcal{E} = 2.475$  MeV,  $\bar{v}_\mu^2 = 1.00)$ , ( $\bar{X}_{\mu\nu}^2 - \bar{Y}_{\mu\nu}^2 =$

<sup>5</sup> <sup>88</sup>Ni has a small IV peak at the IS peak.

0.79) and that with the next largest is  $\pi 2d_{5/2}(\mathcal{E} = 3.654 \text{ MeV}, \bar{v}_\mu^2 = 0) \otimes \pi 1g_{9/2}(\mathcal{E} = 2.276 \text{ MeV}, \bar{v}_\mu^2 = 1)$ , ( $\bar{X}_{\mu\nu}^2 - \bar{Y}_{\mu\nu}^2 = 0.09$ ). This excitation is mainly a single neutron particle and neutron hole. Still, the proton contribution is much larger than that in other channels at the neutron drip line. This excited state has 23.7 % of the total IS strength and 8.6 % of the EWSR.

We see both in this channel and others that the large transition strength near the neutron drip line does not always indicate the coherent contributions of many two-quasiparticle excitations (i.e., collectivity). Yet the transition densities make these strong low-lying states, particularly in Ni and Sn, look very much like the surface vibrations that characterize nuclei closer to stability. To get a better handle on the degree to which the states we examine here can be called vibrations, we show in Fig. 47 the energy, transition probability  $B(E2; 0^+ \rightarrow 2^+)$ , and largest  $\bar{X}_{\mu\nu}^2 - \bar{Y}_{\mu\nu}^2$  for neutrons in the lowest-energy  $2^+$  states of Ca, Ni, and Sn. The Ca panel shows, first of all, that we do not reproduce experimental data very well except in a few nuclei, and second, that the states are dominated by a single two-quasiparticle excitation for  $N \leq 34$ . For  $34 \leq N \leq 40$  something peculiar happens; when the energy increases, so does the  $B(E2; 0^+ \rightarrow 2^+)$ , and vice versa, with the largest  $\bar{X}_{\mu\nu}^2 - \bar{Y}_{\mu\nu}^2$ , a measure of collectivity, varying irregularly. In nuclei with collective vibrations, transition strength is usually correlated inversely with energy [37, 38]; we see the opposite here. Near the neutron drip line of Ni, the classic signs of increasing quadrupole collectivity — decreasing energy, rising  $B(E2; 0^+ \rightarrow 2^+)$ , and decreasing maximum  $\bar{X}_{\mu\nu}^2 - \bar{Y}_{\mu\nu}^2$  — are all present. The Sn isotopes look much more familiar, exhibiting the usual trends, except at the magic numbers. And the states close to the drip line with  $96 < N < 124$  are as classically collective as (or more so than) those in more stable isotopes with  $56 < N < 68$ .

Finally we show the interaction dependence of the collectivity measures for the lowest  $2^+$  states in Sn (the easiest chain to understand) in Fig. 48. In the mid-shell region, the energies are low, the  $B(E2; 0^+ \rightarrow 2^+)$ 's are high, and the largest amplitudes low, as expected from systematics in stable nuclei in regions of large dynamical deformation. The values of these quantities depend significantly on the interaction, however. Ca and Ni show similar behavior but with more irregularities.

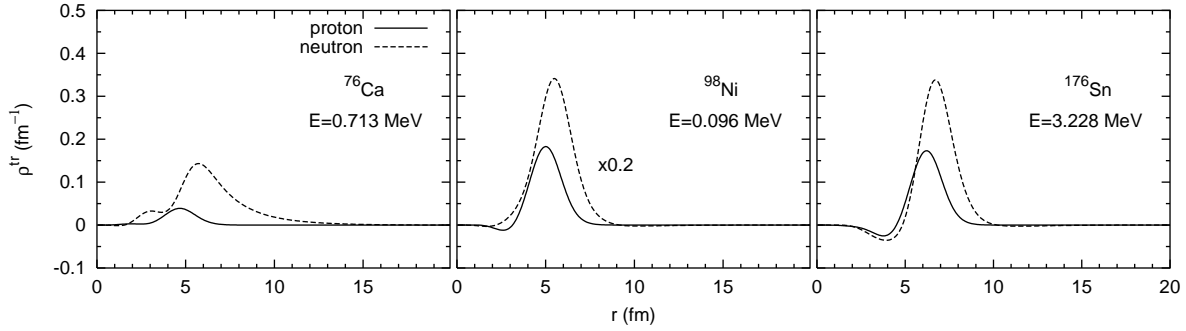


FIG. 45: Transition densities to the excited states in the low-energy peak of the IS  $2^+$  strength functions in the neutron-drip-line nuclei (with SkM\*)  $^{76}\text{Ca}$ ,  $^{98}\text{Ni}$ , and  $^{176}\text{Sn}$ . Both proton and neutron curves are reduced by a factor of 5 in  $^{98}\text{Ni}$  to fit on the figure..

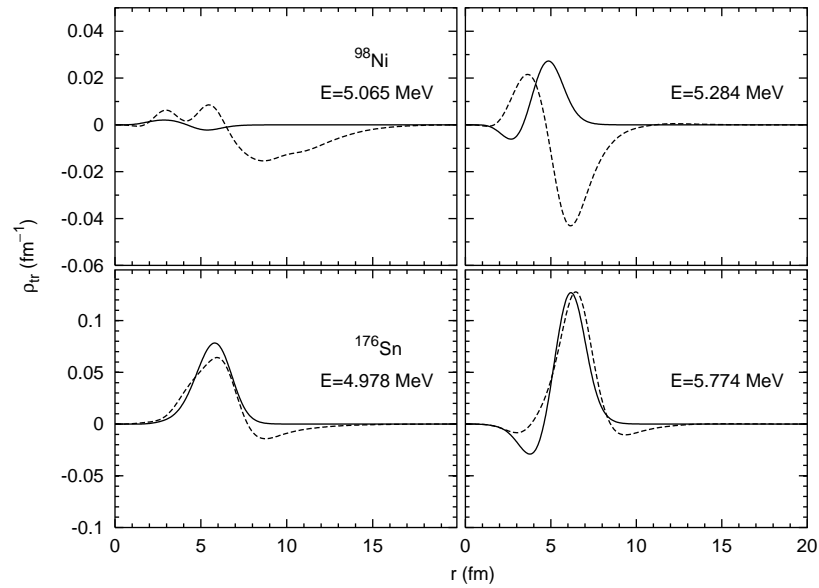


FIG. 46: Transition densities to the excited states in the low-energy peak of the IV  $2^+$  strength functions (SkM\*) in  $^{176}\text{Sn}$  and  $^{98}\text{Ni}$ .

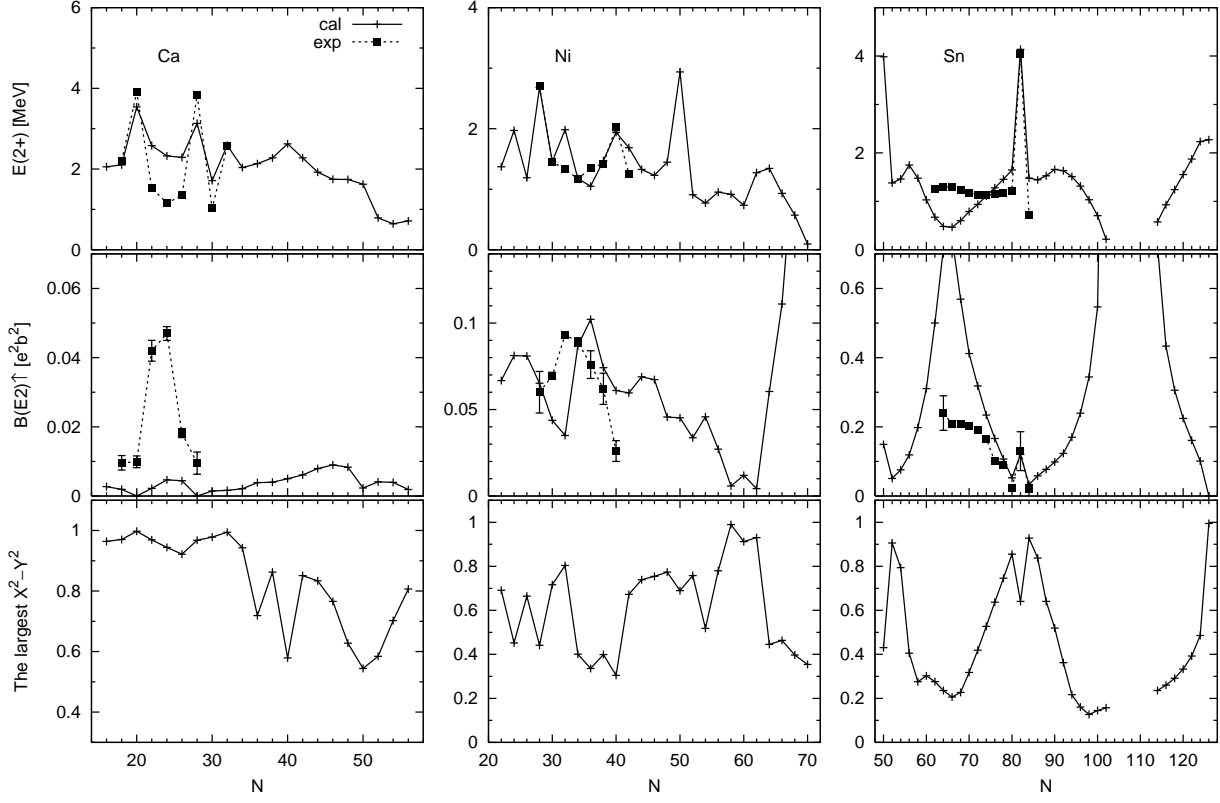


FIG. 47:  $N$ -dependence of the energy (upper),  $B(E2; 0^+ \rightarrow 2^+)$  (middle), and largest  $\bar{X}_{\mu\nu}^2 - \bar{Y}_{\mu\nu}^2$  (lower) of the lowest  $2^+$  states in Ca, Ni, and Sn, with SkM\*. Experimental data are also shown where available.

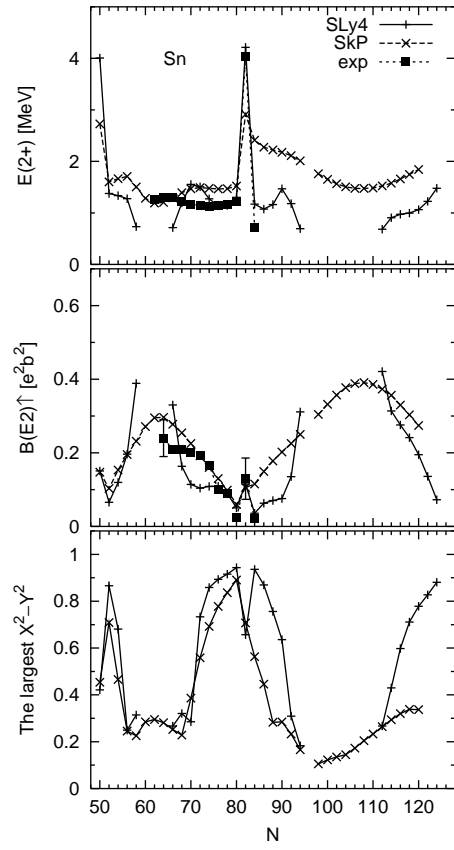


FIG. 48: The same as Fig. 47 but for Sn only, SLy4 and SkP.



## V. CONCLUSION

The feature that leaps out of our calculations is the enhancement of low-energy strength as the neutron drip line is approached. It is present in all multipoles (and is most pronounced in the IS  $1^-$  channel, where the transition operator contains a factor  $r^3$ ), with all Skyrme interactions, and in every isotopic chain, beginning just after a closed neutron shell. Interestingly, the recent measurement of an IV  $1^-$  strength function at GSI shows a low-energy peak before a closed shell, in  $^{130}\text{Sn}$ . This may be due to correlations not included in the QRPA.

The transition densities to the low-lying states reveal some interesting features. In the  $0^+$  and  $1^-$  channels, the low-energy peaks are usually created essentially entirely by a single two-neutron-quasiparticle configuration. In the  $0^+$  channel, where the total number of two-quasiparticle configurations is restricted, even small admixtures of two-proton-quasiparticle states are absent; the proton transition density is nearly zero. Protons play a noticeably larger role in the transition density of the  $1^-$  channel despite the lack of any two-proton-quasiparticle configurations with sizable amplitude. In both these channels, the transition densities have a peak around the rms radius and very long tail outside the radius, which allows single quasiparticle configuration to have such large strength.

The transition densities to  $2^+$  states are different; they have no real nodes and a proton component that is of the same order as the neutron component. The transition densities near the neutron-drip line resemble those of surface vibrations, and in many cases the corresponding states clearly are vibrational. But the usual systematics of collective vibrations is not always present; energies and  $E2$  strengths are sometimes correlated in the wrong way.

Some of the most significant differences in the predictions of the three Skyrme interactions we used are in static properties: the locations of the neutron drip line and quadrupole-deformed regions. But some dynamical properties also depend significantly on the interaction, most notably (and easiest to measure) the energies of and transition-strengths to the lowest  $2^+$  states near regions of deformation and the total energy-weighted IV strength.

This paper, in a way, is a catalog of predicted dynamic properties of nuclei near the drip line. For the most part we have not offered simple explanations for the anomalies that appear. That, we hope, will be the subject of a future paper.

### Acknowledgments

This work was supported in part by the U.S. Department of Energy under grant DE-FG02-97ER41019. We used computers belonging to the National Center for Computational Sciences at Oak Ridge National Laboratory and Information Technology Services at University of North Carolina at Chapel Hill. Parts of this research were done when one of us (J.T.) was at the University of North Carolina at Chapel Hill and at RIKEN.

### APPENDIX: TRANSITION DENSITY

The transition density is defined by

$$\rho_{\text{tr}}^q(\mathbf{r}; k) = \langle k | \sum_{i=1}^{N_{\text{or}}Z} \delta(\mathbf{r} - \mathbf{r}_i) | 0 \rangle, \quad (\text{A.1})$$

where  $|0\rangle$  and  $|k\rangle$  denote the ground and excited states of the system, and  $\mathbf{r}_i$  in the right-hand side is an operator acting on the nucleon  $i$ . The transition density is evaluated in the QRPA (we omit  $q$ ) as

$$\begin{aligned} \rho_{\text{tr}}(\mathbf{r}; k) = & \sum_{K < K'} \left\{ X_{KK'}^{k*} \left( \psi_{K'}^\dagger(\mathbf{r}) \psi_{\bar{K}}(\mathbf{r}) u_{K'} v_K - \psi_K^\dagger(\mathbf{r}) \psi_{\bar{K}'}(\mathbf{r}) u_K v_{K'} \right) \right. \\ & \left. - Y_{KK'}^{k*} \left( \psi_{\bar{K}'}^\dagger(\mathbf{r}) \psi_K(\mathbf{r}) v_{K'} u_K - \psi_{\bar{K}}^\dagger(\mathbf{r}) \psi_{K'}(\mathbf{r}) v_K u_{K'} \right) \right\}, \end{aligned} \quad (\text{A.2})$$

where  $X_{KK'}^k$  and  $Y_{KK'}^k$  are the forward and backward amplitudes of the QRPA solution  $k$  (see Appendix A of Ref. [28]), and  $\psi_K(\mathbf{r})$  stands for a single-particle canonical-basis wave function. The  $uv$  factors associated with the basis are represented by  $u_K$  and  $v_K$ . Assuming spherical symmetry for the system and using

$$\psi_K(\mathbf{r}) = \sum_{m\sigma} R_\mu(r) Y_{l_z}(\Omega) \langle ll_z \frac{1}{2} \sigma | jm \rangle | \sigma \rangle, \quad (\text{A.3})$$

with  $K = (\mu m) = (nljm)$  a set of quantum numbers,  $R_\mu(r)$  a radial wave function, and  $|\sigma\rangle$  a spin wave function, one can derive

$$\begin{aligned} \rho_{\text{tr}}(\mathbf{r}; k) = & \sum_{\mu \leq \mu'} \frac{1}{\sqrt{1 + \delta_{\mu\mu'}}} \sqrt{(2j+1)(2j'+1)} R_{\mu'}(r) R_\mu(r) \\ & \times (-)^{j+\frac{1}{2}} \frac{1}{\sqrt{4\pi}} \begin{pmatrix} j' & j & J_k \\ -1/2 & 1/2 & 0 \end{pmatrix} \frac{1}{2} (1 + (-)^{l'+l+J_k}) Y_{J_k M_k}^*(\Omega) \\ & \times ((-)^{J_k} v_{\mu'} u_\mu + v_\mu u_{\mu'}) (\bar{Y}_{\mu\mu'}^k + (-)^{J_k} \bar{X}_{\mu\mu'}^k), \end{aligned} \quad (\text{A.4})$$

where  $\mu' = (n'j'l')$ , and  $J_k$  denotes the angular momentum of the state  $k$ .  $\bar{X}_{\mu\mu'}^k$  and  $\bar{Y}_{\mu\mu'}^k$  are the forward and backward amplitudes in the spherical representation.

- 
- [1] T. Kobayashi, S. Shimoura, and I. Tanihata et al., Phys. Lett. B **232**, 51 (1989).
  - [2] G. Bertsch and J. Foxwell, Phys. Rev. C **41**, 1300 (1990).
  - [3] C. A. Bertulani and A. Sustich, Phys. Rev. C **46**, 2340 (1992).
  - [4] M. Tohyama, Phys. Lett. B **323**, 257 (1994).
  - [5] M. Yokoyama, T. Otsuka, and N. Fukunishi, Phys. Rev. C **52**, 1122 (1995).
  - [6] F. Catara, E. G. Lanza, and M. A. Nagarajan et al., Nucl. Phys. A **624**, 449 (1990).
  - [7] I. Hamamoto, H. Sagawa, and X. Z. Zhang, Phys. Rev. C **57**, R1064 (1998).
  - [8] I. Hamamoto, H. Sagawa, and X. Z. Zhang, Nucl. Phys. A **692**, 496 (1999).
  - [9] D. Vretenar, N. Paar, and P. Ring et al., Nucl. Phys. A **692**, 496 (2001).
  - [10] G. Colò and P. F. Bortignon, Nucl. Phys. A **696**, 427 (2001).
  - [11] M. Matsuo, K. Mizuyama, and Y. Serizawa, Phys. Rev. C **71**, 064326 (2005).
  - [12] H. Sagawa and T. Suzuki, Phys. Rev. C **59**, 3116 (1999).
  - [13] Y. Suzuki, K. Ikeda, and H. Sato, Prog. Theor. Phys. **83**, 180 (1990).
  - [14] J. Chambers, E. Zaremba, and J. P. Adams et al., Phys. Rev. C **50**, R2671 (1994).
  - [15] H. Sagawa and H. Esbensen, Nucl. Phys. A **693**, 448 (2001).
  - [16] S. Goriely and E. Khan, Nucl. Phys. A **706**, 217 (2003).

- [17] S. Goriely, E. Khan, and M. Samyn, Nucl. Phys. A **739**, 331 (2004).
- [18] N. Paar, P. Ring, and T. Nikšić et al., Phys. Rev. C **67**, 034312 (2003).
- [19] D. Vretenar, T. Nikšić, and N. Paar et al., Nucl. Phys. A **731**, 281 (2004).
- [20] N. Paar, T. Nikšić, and D. Vretenar et al., Phys. Lett. B **606**, 288 (2005).
- [21] D. Vretenar, A. V. Afanasjev, and G. Lalazissis et al., Phys. Rep. **409**, 101 (2005).
- [22] D. Sarchi, P. F. Bortignon, and G. Colò, Phys. Lett. B **601**, 27 (2004).
- [23] N. Tsoneva, H. Lenske, and C. Stoyanov, Phys. Lett. B **586**, 213 (2004).
- [24] I. Hamamoto, H. Sagawa, and X. Z. Zhang, Phys. Rev. C **56**, 3121 (1997).
- [25] I. Hamamoto, H. Sagawa, and X. Zhang, Phys. Rev. C **53**, 765 (1996).
- [26] G. Colò, P. F. Bortignon, and D. Sarchi et al., Nucl. Phys. A **722**, 111c (2003).
- [27] J. Piekarewicz, nucl-th/0602036.
- [28] J. Terasaki, J. Engel, and M. Bender et al., Phys. Rev. C **71**, 034310 (2005).
- [29] J. Dobaczewski, H. Flocard, and J. Treiner, Nucl. Phys. A **422**, 103 (1984).
- [30] J. Dobaczewski, W. Nazarewicz, and T. R. Werner et al., Phys. Rev. C **53**, 2809 (1996).
- [31] P. Ring and P. Schuck, *The Nuclear Many-Body Problem* (Springer-Verlag, New York, 1980).
- [32] J. Bartel, P. Quentin, and M. Brack et al., Nucl. Phys. A **386**, 79 (1982).
- [33] E. Chabanat, P. Bonche, and P. Haensel et al., Nucl. Phys. A **635**, 231 (1998).
- [34] P. F. Bortignon, A. Bracco, and R. Broglia, *Giant Resonances, Nuclear Structure at Finite Temperature* (Harwood academic pub., Amsterdam, 1998).
- [35] G. Colò, N. Van Giai, and J. Meyer et al., Phys. Rev. C **70**, 024307 (2004).
- [36] P. Adrich, A. Klimkiewicz, and M. Fallot et al., Phys. Rev. Lett. **95**, 132501 (2005).
- [37] L. Grodzins, Phys. Lett. **2**, 88 (1962).
- [38] S. Raman, C.W. Nestor Jr., and P. Tikkanen, At. Data Nucl. Data Tables **78**, 1 (2001).